Dynamic Response of Initially Deformed and Imperfect Bi-stable Microbeams under the Combined Effect of Mechanical Shock Loads and Electrostatic Forces

BY

Jihad Erfan AlQasimi

A Thesis Presented to the
DEANSHIP OF GRADUATE STUDIES

KING FAHD UNIVERSITY OF PETROLEUM & MINERALS

DHAHRAN, SAUDI ARABIA

In Partial Fulfillment of the
Requirements for the Degree of

MASTER OF SCIENCE

In
MECHANICAL ENGINEERING

May 2017

KING FAHD UNIVERSITY OF PETROLEUM & MINERALS

DHAHRAN- 31261, SAUDI ARABIA

DEANSHIP OF GRADUATE STUDIES

This thesis, written by **JIHAD ERFAN M. ALQASIMI** under the direction his thesis
advisor and approved by his thesis committee, has been presented and accepted by the Dean
of Graduate Studies, in partial fulfillment of the requirements for the degree of MASTER OF
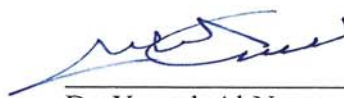SCIENCE IN MECHANICAL ENGINEERING.

THESIS COMMITTEE

Dr. Zuhair Gasem
Department Chairman

Dr. Hassen Ouakad
(Advisor)

Dr. Salam A. Zummo
Dean of Graduate Studies

Dr. Yagoub Al-Nassar
(Member)

29/5/17
Date

Dr. Mehmet Sunar
(Member)

<div dir="rtl">

بِسْمِ اللهِ الرَّحْمنِ الرَّحِيمِ

</div>

"In the name of God, the Most Gracious, the Most Merciful"

<div dir="rtl">

وَفَوْقَ كُلِّ ذِي عِلْمٍ عَلِيمٌ

</div>

″And above every person of knowledge, there is one more learned *(Allah)* ″

<div dir="rtl">

اللَّهُمَّ أعِنِّي عَلَى ذِكْرِكَ، وَشُكْرِكَ، وَحُسْنِ عِبَادَتِكَ

</div>

"Oh God, Help me to Remember You, and

Thank You, and Worship You in the Best of Manners"

<div dir="rtl">

اللُّهم إنِّي أَسْأَلُك عِلمًا نافِعًا، ورزقاً طَيِّبًا، وعَمَلًا متقَبَّلًا

</div>

″O God indeed I ask You for beneficial knowledge,

and Pure Bestowed, and deeds which are accepted″

To my beloved parents

Acknowledgments

First and foremost, I must express my deep gratitude to The Almighty *Allah* for his endless bounties upon me without which I wouldn't reach this position ever.

I also would like to thank my parents *Erfan AlQasimi* and *Yousra Hajjar*, for their limitless love, care and prayers throughout my life. Special thanks are due to my lovely grandma *Jamilah Qabbani*, my brothers and sisters for their continuous support, especially my oldest sibling Dr. *Ahmad* whose help is greatly appreciated.

Next, I would like to express my appreciation to my adviser Dr. *Hassen Ouakad* for his patience and guidance throughout my masters program. Also, I would like to thank Dr. *Yagoub AlNassar* and Dr. *Mehmet Sunar* for their acceptance to be part of my evaluation committee and their fruitful suggestions. Also, an exceptional thank to Dr. *Mahmoud Sarhan* for his inspiration throughout my academic career.

Warm thanks are also extended to my best friends *Abdulrahman Niazi* and *Ahmad Samarqandi* for their true and kind friendship and for giving me hope in my difficult times.

Table of Contents

List of Figures

List of Tables

Abstract

Full Name : Jihad Erfan M. AlQasimi

Thesis Title : Dynamic Response of Initially Deformed and Imperfect Bi-stable Microbeams under the Combined Effect of Mechanical Shock Loads and Electrostatic Forces

Major Field : Mechanical Engineering

Date of Degree : May 2017

This thesis investigates the influence of sudden drop tests on the nonlinear structural behavior of electrically actuated bi-table shallow Micro-Electro-Mechanical-Systems (MEMS) arches. The assumed structure consists of an initially bell-shaped doubly clamped microbeam with a rectangular cross-section. The Euler-Bernoulli beam theory is assumed to represent the nonlinear structural behavior of the bi-stable system under the combined effect of both the DC actuating load and the shaking waves. Moreover, the structural model takes into account both geometric mid-plane stretching and electric actuation nonlinear terms. A multi-modes Galerkin based decomposition is used to discretize the beam equations in order to extract a reduced-order model (ROM). The convergence of the ROM simulations is first verified and furthermore compared to an ANSYS based finite-element simulations in addition to published experimental data. A thorough ROM parametric study showed that the effect of increasing the shallow arch initial rise alter drastically the system behavior from undergoing an uninterrupted snap-through motion to a sudden snap-through instability. Moreover, the influence of the micro-arch beam's initial rise value on its shock spectrum response was investigated. It was concluded that as the micro-arch initial rise value increases, it causes the bi-stable system to collapse under the combined DC and shock wave loadings if the shock wave duration is assumed to be lower or near the system's fundamental natural period. All the presented graphs in this investigation represent some robust

numerical approaches and design tools to help MEMS designers in improving both the reliability and efficiency of these bi-stable based micro-devices under shaking dynamic environments.

ملخص رسالة الماجستير

إسم كاتب الرسالة: جهاد بن عرفان بن محمد القاسمي

عنوان الرسالة: أثر إنحناء االجسور المجهرية على استجابتها للحركة تحت تأثير الصدمات الميكانيكية والقوة الكهربائية

التخصص: الهندسة الميكانيكية

تاريخ الدرجة العلمية: شعبان 1438 هـ

في هذة الرسالة، تمت دراسة نوع من الأنظمة الحديثة المعروف علميا بإسم (ميمز) حيث انها كلمة باللغة الانجليزية تعني الأنظمة الكهروميكانيكية المجهرية. وكلمة مجهرية تشير الى الجزء من مليون، وبالتالي هذه الانظمة متناهية في الصغر. وبسبب صغرها، يصعب التنبؤ بحركاتها تحت تأثير الصدمات المفاجئة، وعادة ما يحصل بعض العيوب أثناء مرحلة التصنيع التي لا يمكن تفاديها. أحد هذه العيوب هو انحناء الجسور المجهرية التي يتم تصميمها على ان تكون مستقيمة تماما. ولكن بسبب عدة عوامل يصعب التحكم بها كالحرارة وغيرها، يحصل هذا الانحناء مما يؤدي الى تغير بعض خصائصها كمدى تحملها للصدمات ومقدار الإنحراف عن موضع السكون. وبسبب صغر هذه الانظمة فإن الكثير من العلاقات توصف بالغير خطية ولها عدة طرق للحل. وقد تم استخدام طريقة تسمى نموذج الدرجة المخفضة، حيث يتم اشتقاق نموذج الدرجة المخفضة باستخدام طريقُة "جاليركن"، بحيث يتم افتراض وضعية الأشكال كدوال أساسية للإشتقاق. وفي هذة الرسالة تمت كتابة بعض الخوارزميات التي تقوم بتوقع درجة إنحراف الأنظمة الكهروميكانيكية والتي من خلالها نستطيع تحديد ما اذا بالامكان استخدام هذه الأنظمة فيما نريد من تطبيقات ام لا. وقد تم استخدام برنامج (ماثيماتيكا) في كتابة الخوارزميات وتم التحقق من النتائج عن طريق مقارنتها مع ما نشر في السابق من أبحاث وتجارب مخبرية في بعض المجلات العلمية. كما أنه تمت المقارنة مع برنامج المحاكاة الهندسي (أنسز) وكانت النتائج متوافقة ومتطابقة. وقد تم إستنتاج عدة أمور مثيرة للإهتمام كتغير سلوك الجسور المجهريه من كونها صلبة الي أن تكون لينة في ظروف معينه مما يؤدي لتغير استجابتها تماما وقد تؤدي الى اتلاف الجهاز في بعض الحالات القصوى. كما نأمل أن يتم استخدام هذة النتائج في تطبيقات مستقبلية لتحسين الاداء والقدرة على تحمل الصدمات بدون أي تلف أو قصور بالعمل بإذن الله تعالى .

Chapter 1 : INTRODUCTION

Micro-Electro-Mechanical-Systems (MEMS) or sometime called micro-systems or micro-machines are devices and structures of distinguished properties and unique characteristics such as small size and low cost of manufacturing [1]. These tiny devices were first invented in the 20th century and then from that time and forward, MEMS designers are improving those tiny devices due to the sudden increase of their reputation. The reason behind this rapid and increasing interest are many such as, their superior electrical and mechanical properties, compact size, low cost of fabrication and can applied in many domains. The domains of such devices are tremendous in all life aspects such as thermal, fluidic, electrical, mechanical, medical, etc... [2-4]. These tiny devices can be practical in many applications such as in sensors and transducers [1, 2], inkjet printers [5], cell phones [6], modern TV's [7], transportation machines (cars, airplanes, etc...) [8], navigation GPS devices [9], micro-pumps [10] and so on... Moreover, because of the fast development and ease in fabrication of such devices, their applications will see more room in our daily life use. MEMS devices fabrication processes consist of numerous methods, such as top-down process and bottom-up method [3, 4]. Nonetheless, and in general, they undergo many processes, and to cite few: the successive deposition, and the doping and etching of thin materials [11]. These processes can be made in term of large batches at once and therefore make their effective cost much lower.

As mechanical engineers, we should consider several other factors that may influence the operation of these MEMS devices during their manufacturing process or even when designing them, such as their materials selection, their actuating forces (electromechanical), the surrounding un-controlled vibration, as well as their resultant reliability and durability. Other

1

significant factors can be the surface forces such as adhesion, friction, meniscus forces, and the viscous damping forces. These are mainly due to their large surface to volume ratios [3]. In addition that these small devices do not use any traditional lubrication [12].

1.1 Motivation

MEMS devices can undergo high sensitivity by changing some of their key design parameters. These parameters depend mainly on the basic structures from which MEMS devices are made of such as microbeams. For example using MEMS in applications such as resonant sensor [13] and RF switcher and filters [14] require high sensitive components such as microbeams. This can be achieved through having a higher natural frequency, which mainly depends on the material property of these micro-structures, its initial condition and its boundary conditions. In general, clamped-clamped boundary conditions for microbeams have high natural frequencies in comparison to other designs such as clamped-free (cantilever) beams, and pinned-pinned beams. Moreover, microbeams form the basic elements in building MEMS device. They can have different structural types such as clamped-clamped and clamped-free [1]. Each type will have its own properties that make it best fit in its respective application. Such properties are their high or low power consumption, their switching time, their pull-in voltage and their response under different loads. Furthermore, more complicated shapes can be considered such as double or triple microbeams on top or aside each other. Other types can be designed by attaching rigid paddle or mass at the tip of cantilever this will lead to different properties and natural frequency [15, 16]. Others can also be realized via using composite material layers to build some basic microbeams based MEMS devices [17].

One of the most interesting structures in numerous MEMS applications are shallow arches. These shapes are either made intentionally or in most cases due to some imperfections in the manufacturing that result into an initial curvature in straight microbeams [18]. Unexpected initial curvature in straight microbeams can lead to many problem such as low reliability, stiction and undesired failure. Therefore, studying carefully the reliability of MEMS arches can represent a key point of correctly designing them to be robust and reliable. The main objective of this research is to investigate mathematically and numerically the reliability phenomena that MEMS arches can undergo under several forces such as mechanical shock load as electric actuating forces. In the following section, few published investigations will be discuss regarding the response of arched micro clamped-clamped beam under different types of loading.

1.2 Literature Review

The importance of investigating both the linear and the nonlinear dynamics of MEMS based microbeams will help engineers to establish optimum operating linear regimes applications. Moreover, nonlinear behavior became important because of the potential for new applications that needs nonlinear phenomena. This unpredictable response mare mainly influenced by many factors such as high shock load, large actuating forces and geometric nonlinearity along the clamping boundaries. This will be a consequence for a nonlinear damping that makes the problem much difficult to be described [19, 20].

1.2.1 Common Reliability Issues in MEMS

The definition of reliability of a designed mechanism is its adequacy or state of being trustworthy to perform its tasks without any possible failure. Furthermore, it is the aptitude to produce same result in certain test or experiment on repeated trials without undergoing any failure state. Accordingly, reliability is one of the key factors in evaluating any future products.

In general, MEMS reliability can be affected by many factors such as any assumed temperature gradient, any presumed relative humidity, the types of actuation (electric, magnetic, piezoelectric, thermal), the packaging and material selection, etc... Although MEMS are similar to the integrated circuits (ICs) in their manufacturing processes with only few differences in their 3D drawings features in MEMS while 2D drawings are assumed in ICs. Packaging process for ICs is well established and developed nowadays. On the other hands, MEMS packing is still under development due to their complex structures and specific performances. Material selection for packing these micro devices is also a major concern in the MEMS reliability where undesired stresses can be developed in the process. In addition, vacuum packaging is advisable to prevent any cause of moist absorption, which can cause failure. Relative humidity in both manufacturing and operating environment can affect MEMS reliability by causing delamination and failure at the end. Failure can be categorized into fracture, creep, stiction, electro migration, wear and pitting of contacting surfaces, etc… [21, 22]. Reliability of MEMS devices can also be affected by their actuating forces type. For example, operating MEMS at high resonant frequencies can cause mechanical fatigue for the different components, which can hence result in cracks initiation and propagation. Thermal fatigue can also play central role against thermal reliability of MEMS devices. MEMS devices subjected to relevant temperature gradient will result in a thermal cycling with high temperature profile leading to the creep of the device [23]. Stiction is an important design factor because it is unavoidable in numerous MEMS applications relying on parallel-plates electric force as actuating technique. In fact, in smaller scale devices surface forces become increasingly dominant and can hence cause stiction of the structure in the micro and nano scales. These surface forces consist mainly of capillary forces, the molecular Van Der Waals forces, and the electrostatic forces which were reported by several research groups such as

4

[21, 22]. Some of these forces, such as the capillary forces, are introduced during certain processes such as during dry processes [24, 25].

Concerning the wear reliability of MEMS devices, adhesive wear was identified as a major cause of failure for silicon based micro-systems in comparison with abrasive and corrosive wear. This wearing problem is mainly due to some broken asperities accumulated at the MEMS surfaces as wear debris particles. An analytical model has been developed to predict the number of cycles to failure of certain tested MEMS devices as a function of actuating voltage and frequency [26].

Finally and regarding the general reliability issues that may influence the effectiveness of MEMS devices, we propose next to discuss the environmental effects on the MEMS devices reliability. Principally we will limit our subsequent discussion on the temperature gradient and relative humidity effects. It is worth mentioning that some military applications require reliable sensors under huge thermal storage conditions along with high-g environments. Such application are missiles, space sensors and automotive airbags [27]. It was found that creep phenomena could occur in MEMS sensors at these huge temperature situations. This temperature gradient depends on the material type of the used MEMS sensor. Creep is one of the major concerns in RF MEMS and micro-mirror devices [28]. Former investigations showed that RF switches having high moment of inertia could withstand higher thermal stress. Thus they are sensitive in high frequency and power situations [29]. Most of the MEMS applications are not operating under vacuum conditions, thus relative humidity cannot be ignored. Studies showed that relative humidity resulted in anodic oxidation, which expands, delaminates and pushes against the bottom of the suspended beams. Moreover mechanical failures resulted from the initiated cracks formed by such oxidation transformation [30].

1.2.2 Reliability of MEMS under Mechanical Shock Waves

Reliability of MEMS under vibratory and shaking environments was investigated up to couple of thousand time of the gravitational acceleration constant *g*. In this regards, several studies modeled these tiny structures as microstructures attached to elastic substrates with applied shocks assumed as pulses of acceleration with finite time duration. It was concluded that if shock duration longer than few millisecond, the MEMS structure will behave as rigid body with low probability to be affected by stress-wave-induced damage [31]. Moreover, MEMS were shown not to be significantly affected by air-damping or squeeze-film damping. It was demonstrated that MEMS failure can be caused either in terms of a critical stress or by any sever displacement [31].

Another valid failure process that can MEMS device undergoes is the quasi-static fracture even in atypical dynamic environments experienced [31]. Furthermore, efficient computational models has been developed to study the dynamic response of microbeams using Galerkin-based reduced-order model and a hybrid approach for spring mass damper system with static and dynamic combination of shock load [29]. The outcomes of these numerical models were then compared with finite element, analytical models and experimental data [29, 32]. It was concluded that these numerical models represent was an efficient method to describe the behavior of microbeams under quasi-static and dynamic loading conditions [29].

To cite an actual example of a MEMS device, the reliability of micro-gyroscopes was investigated under different type of shock loads with varying duration, magnitude of the load and damping conditions by both numerical and experimental methods. The result was highly dependent on the MEMS devices natural frequencies and more importantly air-damping (vacuum

condition). It was notable that changing the direction of the shock load resulted in different failure mechanisms [33].

Other scientists [34] tested bi-stable switch devices under temperature shock, humidity and ballistic shock after packaging. The device was able to resist ballistic shock to max value of 30,000g and humidity test, until it was reported physically broken. Then, shock impact reliability and failure for MEMS micro-gyroscope was tested at three different impact orientations and various acceleration magnitude of shock impact, ranging from 1,500g to 15,000g [35]. The experimental observations shows two type of failures, package failure and functional failure was noticed around 4,000g and 8,000g respectively [35]. Furthermore, simulation investigations of the stress distribution and deformation of the structure were used to predict both potential failure and possible stiction locations inside the MEMS [35]. Certain MEMS devices were also tested under in situ impact with acceleration over 120,000g. The reported results showed a linear relationship with respect to the traditional drop testing [36].

A new method was developed in order to protect MEMS devices from shaking environments [37]. This new reported technique showed more efficient reliability of MEMS devices in comparison with the old protective techniques such as hard stopper and compliant spring stopper [38, 39]. This new method consists of compliant latching stopper mainly designed to reduce the impact force applied on the microstructures. In addition, its effectiveness was verified experimentally. This design works simply by dissipating large amounts of energy via a latching mechanism. Moreover, this compliant latching stopper does not requires extra fabrication process. It can be manufacturing along with the movable structures of the main devices [37]. In addition, experimental and theoretical work has been performed on testing the connection between the motion of the printed circuit board (PCB) and the MEMS devices [40].

Low pulses were assumed to simulate table drop, applied on the base of MEMS-PCB assembly. Simulation data showed the effects of the natural frequency for both MEMS and PCB along with duration of shock pulse [40]. The result displayed that poor PCB design will lead to more dynamical instabilities and therefore squeeze film damping would have more effect on the mechanical shock load and hence stabilizing the MEMS device [40].

1.2.3 MEMS Shallow Arches

MEMS shallow arches has been one of the important design in the micro scaled devices community for several reasons. One of them is because when fabricating microbeams curvature is almost inevitable which is caused mainly because of the imperfections that arise during MEMS micro-fabrication processes. Therefore, several research studies [41-49] investigated the effect of initial curvature on the structural and dynamical behavior of MEMS arches. In fact, the nonlinear structural and dynamical behavior of MEMS arches was theoretically modeled through numerous discretization techniques such as the Galerkin reduced order modeling, finite-difference models, finite-elements models, the differential-quadrature method, etc… [50, 51]. Experimental works showed interesting softening and hardening behavior of arched microbeams near the first and third natural frequencies, respectively [41-49]. A two dimensional high order expression was developed out of elasticity equations into Legendre's polynomials series. These equations were used to study the pull-in instability and stress–strain state of fixed–fixed and simply supported arched micro-beams. To insure their model validation, a comparison with a COMSOL Multiphysics finite-element analysis was assumed. The comparison showed an excellent matching between the two approaches [52].

Furthermore, the static and dynamic behavior of an electrostatically actuated clamped–clamped curved microbeam were studied [53]. It was concluded that curved deformations were

mainly caused due to stress gradient of the microbeam and its flexible anchors. The experimental data revealed several nonlinear phenomena such as jumps, hysteresis, and softening behaviors [53]. Reduced order models (ROMs) were constructed to investigate the static behavior of clamped-clamped arched microbeam under small DC electric load and an AC harmonic load. On the other hand, perturbation method was used to simulate dynamic response under different DC and curvature values [54]. Effective non-linearity and non-linear resonance frequencies are calculated as function of initial curvature [54]. The results shows softening for all loads and initial rise values [54]. A multi-modes Galerkin based reduced order modeling was developed to examine the nonlinear behavior of arched double clamped microbeam excited by DC electrostatic load superimposed to an AC harmonic load [55]. The result come out to have softening and hardening behavior when it is close to the first and third resonance frequency respectively. The developed model predicted these behaviors perfectly with slight discrepancies [55]. Pull-in characteristics for arched microbeam actuated by harmonic AC along with DC voltage was investigated numerically by using ROM. The result showed increase of pull-in at high DC voltage and it's amplitude if width is increased or by decreasing the height of the microbeam [56].

Additionally, electric fringing-fields effects were studied using ROM for clamped-clamped arched microbeam [57]. The developed model was numerically solved assuming Newton–Raphson method and compared to experimental data as well as finite element program (ANSYS). It was reported that if the fringing-fields effects was not included it will caused significant errors in static deflection and snap-through and pull-in voltages [57]. Additionally, the combined effect of curved geometry and fluid squeeze-film damping (SQFD) is investigated using ROM. The result shown the effect of SQFD on convex and concave microbeams. It was

9

noticeable that frequency response and the snap-through values were changing in case of convex, while it was less in case of concave type microbeam. Moreover, peak resonant values was affected by air micro-gap [58].

According to the above-discussed literature, reliability represents a crucial issue in the design process of MEMS devices, which mainly motivated many researchers to study these aspects and how they can help improving their overall robustness. However, most of the available studies focused on varying one external load force for instance temperature, pressure difference, humid conditions, etc… without focusing on any kind of simultaneous effect. Therefore, in order to enrich the state of the art, we propose in this work to investigate the combined effect of different loads at the same time on the reliability of MEMS devices. Our main focus will be on the combined effect of electrostatic DC actuation along with a mechanical shock wave on the structural response of a MEMS shallow arch.

1.3 Thesis Objectives and Organization

The objectives of this thesis are the following:

- ✓ To summarize previous numerical investigations on the structural behavior of MEMS based shallow arches.
- ✓ To derive the equation of motion using the extended Hamilton principle and establish the continuum model to simulate the behavior of shallow arches under the combined effect of mechanical shock waves and electrostatic forces.
- ✓ To develop a reduced-order model using a modal decomposition method and derive a set of ordinary differential equations and solve them numerically using a 4th order Runge-Kutta scheme.

✓ To simulate the same model using finite element methods (FEM) under different shock and electric loads.

✓ To investigate, through a detailed parametric study (force and shock spectrum analysis), the nonlinear vibrational behavior of MEMS shallow arches under mechanical shock and electric loads.

Consequently, the organization of this thesis is as follows. In the second chapter, we will present a brief background on the beam model problem formulation of micro shallow arches, then introduce the different types of external forces which will be considered on this investigation. Chapter 3 will focus on presenting the Galerkin reduced-order model (ROM) modal decomposition technique as applied to discretize the shallow arch nonlinear beam equation of motion. In the same chapter, we will also expose some details on how to solve the shallow arch linearized eigenvalue problem, ascertain the convergence of the modal expansion technique, and finally validate the numerical results of the modal analysis. Next, in Chapter 4, we will examine the response of clamped-clamped shallow micro-arch beam under pure mechanical shock wave and electrostatic DC load independently. Chapter 5 will summarize, through a comprehensive parametric study, the results of the combined effect of mechanical shock waves and electrostatic loads on the structural behavior of shallow arch microbeam. Finally, some conclusions and recommendations for future work will be summarized in Chapter 6.

Chapter 2 : BACKGROUND

The purpose of this chapter is to derive the equation of motion of arched microbeam under half sine shock load. Then, a reduced-order model (ROM) discretization technique assuming a Galerkin based modal decomposition technique will be carried out. Next the outcome of the ROM will be used to numerically solve the shallow arch nonlinear Euler Bernoulli microbeam equation of motion.

2.1 Nonlinear Structural Euler Bernoulli Beam Model

This section focus on deriving the equation of motion (EOM) of initially curved clamped-clamped beam along with its boundary conditions using Hamilton's principle. The theory assumed for modeling the beam structural behavior as the Euler-Bernoulli beam theory. This assumption has been made while bearing in mind that the beam cross-sectionals planes will remains parallels even after deformations. Figure 2.1 shows the assumed initially curved microbeam with an initial shape designated by its first Euler buckling instability shape function $\hat{w}_0(\hat{x}) = d_0\left(1 - \cos(2\pi\hat{x}/L)\right)/2$, where the arch maximum (mid-point) initial rise d_0, a length L, width b, thickness h and distance from the electrode of value d. In addition, by assuming that the beam posses a cross section area $A = bh$, a Young's modules E, a mass density of ρ and a second moment area of $I = bh^3/12$. Also assuming that the arched beam is subjected to constant axial force of magnitude N as shown below in Figure 2.2. While considering the function $\hat{w}(\hat{x},\hat{t})$ to represent the transverse displacement of the beam from its initial position profile $\hat{w}_0(\hat{x})$. Furthermore, the function $\hat{u}(\hat{x},\hat{t})$ is considered to represents the axial displacement of the arched beam.

12
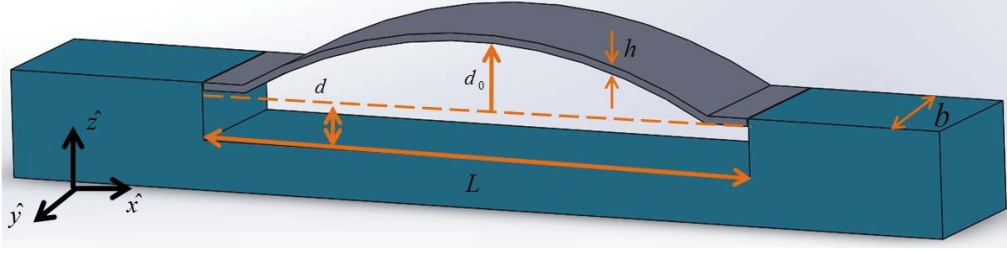
Figure 2.1: 3D schematic of a shallow micro-arch beam displaying its geometrical properties.
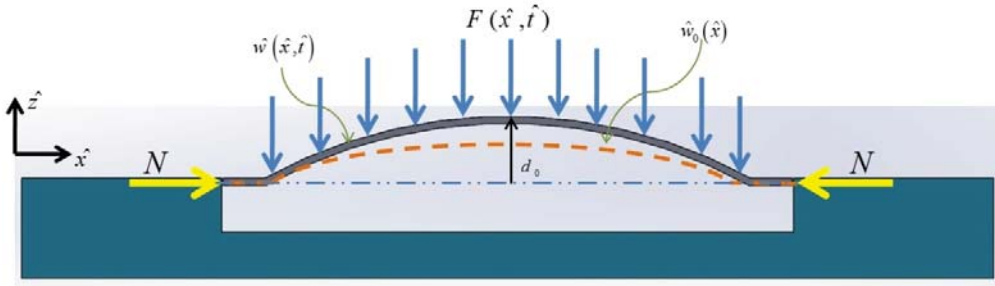
Figure 2.2: 2D (Side view) schematic of a MEMS arched beam showing all forces acting on it.

2.2 External Forces

Here we will provide a brief description on the external forces assumed in this investigation for actuation (the electric force) and the mechanical shock pulse to model a sudden drop test. Additionally, two main structural instabilities of electrically actuated MEMS shallow arches will be discussed: the snap-through and the pull-in instabilities.

2.2.1 Electrostatic Actuating Force

Electrical actuation of MEMS devices is one of the common used method. It relies on parallel plate capacitors. Where voltage source, low power consumption and rapid actuation are the main characteristics for such capacitors. Figure 2.3 shows the schematic view of electrically actuated microbeams.
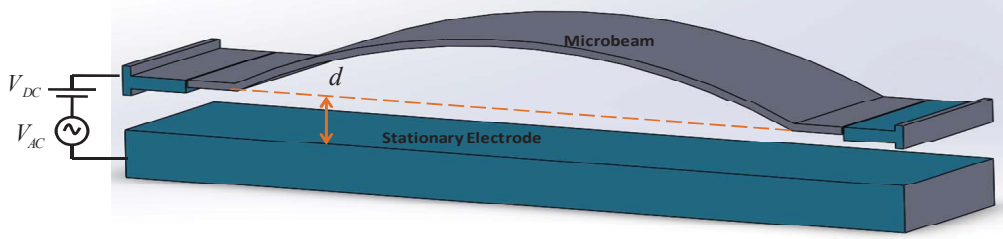
Figure 2.3: 3D schematic of a shallow micro-arch beam displaying its assumed parallel-plates electrosttic actuation technique.

Several studies [50, 51, 59] showed that the initial gap size (*d*) is non-linearly proportional to the magnitude of the attractive forces in between capacitor plates. The mathematical formulation of electro static force per unit length, assuming rectangular cross section of parallel plates, can be represented as [1]:

$$F_{EL}(\hat{x},\hat{t}) = \frac{\varepsilon_0 b \left[V_{DC} + V_{AC} \cos\left(\omega_f \hat{t}\right) \right]^2}{2 \left[d - \hat{w}(\hat{x},\hat{t}) \pm \hat{w}_0(\hat{x}) \right]^2} \tag{2.1}$$

where $\varepsilon_0 = 8.854 \times 10^{-12}$ F.m^{-1} is the permittivity electrical of air and ω_f is harmonic frequency. V_{DC} and V_{AC} are direct and alternating currents amplitudes respectively. (+/-) are picked based on the concavity of the curved beam (+ concave up, - concave down).

2.2.2 The Snap-through and Pull-in Instabilities in MEMS shallow Arches

AC and DC voltages are the main components of electrical actuation as applied in many parallel-plates based capacitors. When a DC load is applied, it causes deflection of plates into a new equilibrium position. A structural instability can be initiated if the applied DC load is exceeding a threshold value, above which the restoring force of the MEMS device cannot anymore withstand the actuating electric force. Consequently, the parallel plates would collapse leading to a short circuit and hence to the device failure. This phenomena is a main failure in electrically actuated MEMS devices and is called static pull-in instability. Figure 2.4-(a) shows

14

the stages for a pull-in instability as the DC voltage is varied [60]. Similarly, dynamic pull-in can be realized when assuming dynamic harmonic AC voltages in MEMS devices [61].

Moreover, Figure 2.4-(b) illustrates another type of structural instability that a MEMS shallow arch can undergo: the snap-through instability. Similar to the pull-in instability, snap-through can be caused by static or dynamic loading. Snap-through appears if the disturbance of the bi-stable microbeams exceeds the initial rise or if it vibrates in between original and symmetric configuration [41].

$$V_{DC} = 0 \qquad\qquad V_{DC} \geq V_{pull-in}$$

(a)

$$V_{DC} = 0 \qquad\qquad V_{DC} \geq V_{snap-through}$$

(b)
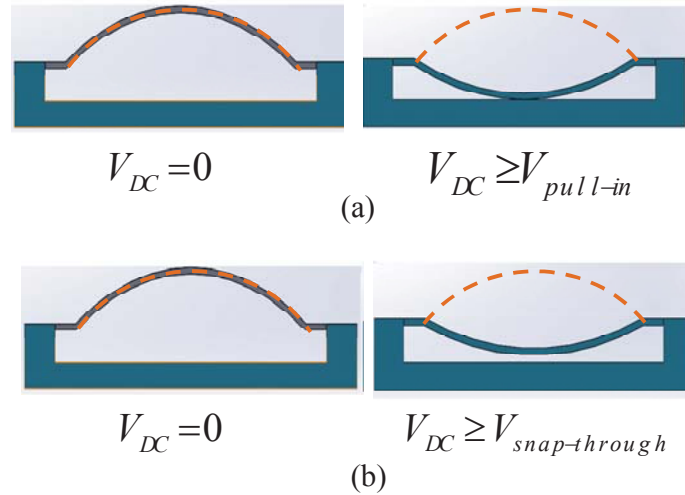
Figure 2.4: Illustration of instabilities scenarios in an electrically actuated shallow micro-arch (dashed line is the original configuration at zero load) (a) Pull-in (b) Snap-through.

2.2.3 Mechanical Shock Waves

A mechanical shock wave can be defined as a suddenly applied stress, velocity, acceleration or displacement over short period of time relative to the natural period of the considered micro-structure. A mechanical shock pulse is characterized by its maximum value (amplitude), duration, and shape (half-sine, unit-step, and saw-teeth, etc...). Mechanical shocks usually cause rapid transformation of energy to the impacted device. The profile of a mechanical

shock force as function of time can have various forms depending on shock source, and material properties of the system. For instance, after many experiments on bombs and explosion, the resultant shock profile can be approximated as initial peak right triangle pulse. Moreover, hammer hit can be assumed as impulse profile whereas shock profile due to dropping can be assumed as half sine profile. In the upcoming sections we will use various type of shock profiles such as half sine, step and saw-tooth, Figure 2.5, to observe the difference in response of the clamped-clamped microbeam [1, 32, 62].
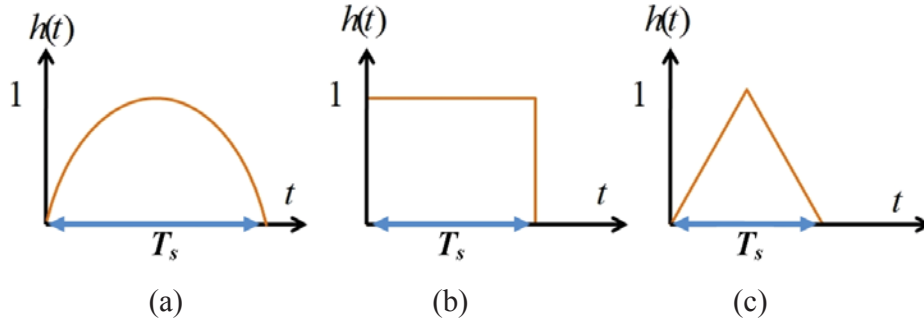
Figure 2.5: Simple shock pulse models. (a) half sine wave (b) unit step wave (c) saw-tooth wave.

The following analytical expressions are representing step, half sine and saw-tooth respectively:

$$h(\hat{t}) = \hat{F}\left[\sin(\omega\,\hat{t})\,U(\hat{t}) + \sin(\omega\,(\hat{t}-T_s))\,U(\hat{t}-T_s)\right] \tag{2.1}$$

$$h(\hat{t}) = \hat{F}\left[U(\hat{t}) - U(\hat{t}-T_s)\right] \tag{2.3}$$

$$h(\hat{t}) = \hat{F}\left[\frac{\hat{t}}{T_s/2} - 2\left(\frac{\hat{t}-T_s/2}{T_s/2}\right)U(\hat{t}-T_s/2) + \left(\frac{\hat{t}-T_s}{T_s/2}\right)U(\hat{t}-T_s)\right] \tag{2.4}$$

where, $U(\hat{t})$ and $U(\hat{t}-T)$ are unit step functions, T_s represents the shock period, $\omega = \pi/T_s$ is forcing frequency and $\hat{F}$ is its respective amplitude. In this thesis, we will mainly focus on half sine representation of the shock wave and its influence on the behavior of MEMS arches.

2.3 Shallow Arch Nonlinear Beam Model

In order to derive the equation of motion of a shallow arch beam in Figure 2.6, by considering the initial position of a point on the beam as A_1 in which it have the coordinates of x_1 in the axial direction and z_1 be the transverse coordinate, as shown in Figure 2.7. The final position of the same point after deforming is A_2 with coordinates x_2 and z_2 in the axial and transverse coordinate. Now by consider a differential element of length dx_1 at point A_1. The point is displaced a distance $\hat{u}$ and $\hat{w}$ in the axial and transverse direction respectively. The element getting deformed to dx_2 and dz_2 axially and transversely.

Using the parameters displayed in Figure 2.7, we can mathematically write that:

$$\begin{cases} x_2 = x_1 + \hat{u} = \hat{x} + \hat{u} \\ z_2 = z_1 + \hat{w} = \hat{w}_0 + \hat{w} \end{cases} \tag{2.5}$$

Through applying the Pythagoras theorem using Figure 2.7, we can derive:

$$d\hat{s} = \sqrt{(dx_2)^2 + (dz_2)^2} \tag{2.6}$$
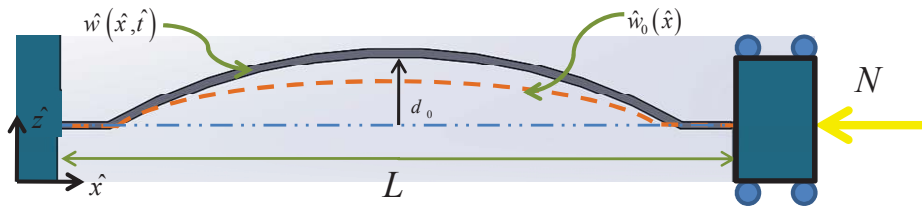
Figure 2.6: Schematic of a clamped-clamped arch beam under a compressive axial load.
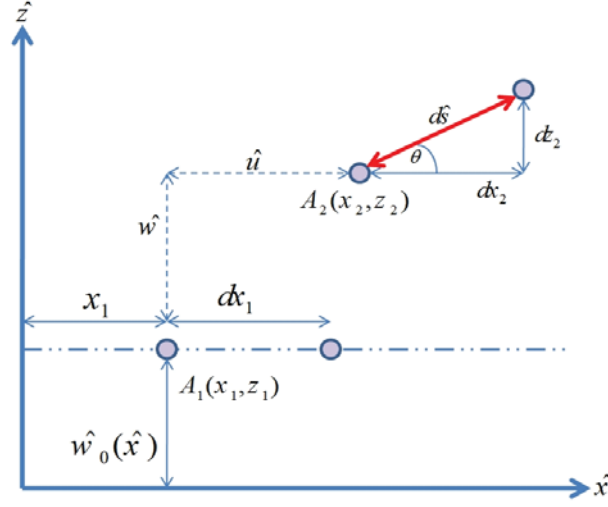
Figure 2.7: A segment of the micro-arch beam after deformation.

Consequently, and using Equation (2.5), we can re-write Equation (2.6) as follows:

$$d\hat{s} = \sqrt{\left(d\hat{x}+d\hat{u}\right)^2 + \left(d\hat{w}+d\hat{w}_0\right)^2} = \sqrt{\left(1+\hat{u}'\right)^2 + \left(\hat{w}'+\hat{w}_0'\right)^2}\,d\hat{x} \tag{2.7}$$

where "'" denotes the first derivative with respect to x.

Then expanding Equation (2.7) we get:

$$d\hat{s} = \sqrt{1 + 2\hat{u}' + \hat{u}'^2 + \hat{w}'^2 + 2\hat{w}'\hat{w}_0'}\,d\hat{x} \tag{2.8}$$

Assuming a shallow arch arrangement, the initial curvature rise slope would be small compared to unity, i.e., $\left(w_0'\right)^2 \ll 1$, therefore the deformed element strain becomes:

$$\varepsilon = \frac{d\hat{s}-d\hat{x}}{d\hat{x}} = \sqrt{1 + 2\hat{u}' + \hat{u}'^2 + \hat{w}'^2 + 2\hat{w}'\hat{w}_0'} - 1 \tag{2.9}$$

Formerly the stretch ratio for the beam element can be calculated as:

$$\lambda = \frac{d\hat{s}}{d\hat{x}} = \sqrt{1 + 2\hat{u}' + \hat{u}'^2 + \hat{w}'^2 + 2\hat{w}'\hat{w}_0'} \tag{2.10}$$

Consequently the angle of rotation in Figure 2.7 is given as:

18

$$\begin{cases} \sin\theta = \dfrac{dz_2}{d\hat{s}} = \dfrac{\hat{w}'_0 + \hat{w}'}{\lambda}, \\[3mm] \cos\theta = \dfrac{dx_2}{d\hat{s}} = \dfrac{1 + \hat{u}'}{\lambda}, \end{cases}$$
(2.11)

Afterward by differentiating Equation (2.11) yields:

$$\theta' = \frac{\left(1 + \hat{u}'\right)\left(\hat{w}''_0 + \hat{w}''\right) - \hat{u}''\left(\hat{w}'_0 + \hat{w}'\right)}{\lambda^2}$$
(2.12)

where " $''$ " denotes the second derivative with respect to x.

The mid-plane curvature for the arched beam can then be computed as:

$$k = \frac{d\theta}{d\hat{s}} = \frac{d\theta}{d\hat{x}}\frac{d\hat{x}}{d\hat{s}} = \frac{\left(1 + \hat{u}'\right)\left(\hat{w}''_0 + \hat{w}''\right) - \hat{u}''\left(\hat{w}'_0 + \hat{w}'\right)}{\lambda^{3/2}} = \frac{\left(1 + \hat{u}'\right)\left(\hat{w}''_0 + \hat{w}''\right) - \hat{u}''\left(\hat{w}'_0 + \hat{w}'\right)}{\left(1 + 2\hat{u}' + \hat{u}'^2 + \hat{w}'^2 + 2\hat{w}'\hat{w}'_0\right)^{3/2}}$$
(2.13)

Using a Taylor Series expansion to for Equation (2.9) up to the quadratic terms for small u' and w' we get:

$$\varepsilon \approx \hat{u}' + \frac{\hat{w}'}{2} + \hat{w}'\hat{w}'_0 + \cdots$$
(2.14)

Therefore, the total axial strain of the beam at a distance z from mid-plane line of the beam is given by:

$$\varepsilon_T \approx \varepsilon - \hat{z}\hat{w}'' + \cdots$$
(2.15)

By using Taylor series expansion for small u' and w' up to quadratic terms the mid-plane beam curvature given by Equation (2.13) can be simplified as:

$$k \approx \left(\hat{w}''_0 + \hat{w}''\right) - \hat{u}''\left(\hat{w}'_0 + \hat{w}'\right) - 2\left(\hat{w}''_0 + \hat{w}''\right)\hat{u}'' + \cdots$$
(2.16)

2.3.1 The Potential Energy

The beam potential energy due to its elastic deformation and its mid-plane stretching is given by:

19

$$V = \frac{1}{2} \int_0^L \int_{-d/2}^{d/2} \int_{-b/2}^{b/2} \left(E\varepsilon_T^2 \right) d\hat{y}\, d\hat{z}\, d\hat{x}$$

$$= \frac{1}{2} \int_0^L \int_{-d/2}^{d/2} \int_{-b/2}^{b/2} \left(E\left\{ \left(\hat{u}' + \frac{\hat{w}'}{2} + \hat{w}'\hat{w}_0' \right)^2 + -\hat{z}\hat{w}'' \left(\hat{u}' + \frac{\hat{w}'}{2} + \hat{w}'\hat{w}' \right)^{=0} + \hat{z}^2\hat{w}''^2 \right\} \right) d\hat{y}\, d\hat{z}\, d\hat{x},$$

$$= \frac{EA}{2} \int_0^L \left(\hat{u}' + \frac{\hat{w}'}{2} + \hat{w}'\hat{w}' \right)^2 d\hat{x} + \frac{EI}{2} \int_0^L \hat{w}''^2 d\hat{x} \tag{2.17}$$

2.3.2 The Kinetic Energy

By ignoring the axial strain, beam's kinetic energy is given as follows [63]:

$$T = \frac{\rho A}{2} \int_0^l \dot{\hat{w}}^2 d\hat{x} \tag{2.18}$$

where the dot denotes partial derivative with time $\hat{t}$.

2.3.3 The Hamilton Principle

The equation of motion of continuous systems and it's boundary condition can be obtained with numerous methods. The Hamilton Principle is one of these methods. It stipulates that for a conservative mechanical system at particular period of time the integral of the Lagrangian (difference between the Kinetic and the Potential energy) of the system is stationary. The principle can be extended to non-conservative systems in the following manner [64, 65]:

$$\int_{t_1}^{t_2} \partial L d\hat{t} = \int_{t_1}^{t_2} \left(\partial T - \partial V + \partial W_e \right) d\hat{t} = 0 \tag{2.19}$$

where the non-conservative work done by the external force denoted by W_e, the elastic potential energy denoted by V, the kinetic energy denoted by T and the Lagrangian of the system denoted by L. The initial and final value of time are t_1, t_2 respectively. Integrating by parts over time Equation (2.17), the potential energy variational operator would be:

20

$$\int_{t_1}^{t_2} \partial V d\hat{t} = \int_{t_1}^{t_2} \left\{ \begin{array}{l} EA\left[\left(\hat{u}' + \dfrac{\hat{w}'}{2} + \hat{w}'\hat{w}_0'\right)\partial\hat{u}\right]_0^L - EA\int_0^L \left(\hat{u}' + \dfrac{\hat{w}'}{2} + \hat{w}'\hat{w}_0'\right)'\partial\hat{u}\ d\hat{x} + \\[2mm] +EA\left[\left(\hat{u}' + \dfrac{\hat{w}'}{2} + \hat{w}'\hat{w}'\right)\hat{w}'\ \partial\hat{w}\right]_0^L - EA\int_0^L \left(\left(\hat{u}' + \dfrac{\hat{w}'}{2} + \hat{w}'\hat{w}'\right)\hat{w}'\right)'\partial\hat{w}\ d\hat{x} + \\[2mm] +EA\left[\left(\hat{u}' + \dfrac{\hat{w}'}{2} + \hat{w}'\hat{w}'\right)\hat{w}_0'\ \partial\hat{w}\right]_0^L - EA\int_0^L \left(\left(\hat{u}' + \dfrac{\hat{w}'}{2} + \hat{w}'\hat{w}_0'\right)\hat{w}_0'\right)'\partial\hat{w}\ d\hat{x} + \\[2mm] +EI\left[\hat{w}''\ \partial\hat{w}'\right]_0^L - EI\left[\hat{w}'''\ \partial\hat{w}\right]_0^L + EI\int_0^L \hat{w}''''\partial\hat{w}d\hat{x} \end{array} \right\} d\hat{t} \qquad (2.20)$$

Integrating by parts over time Equation (2.18), the kinetic energy variational operator can be expressed as follows:

$$\int_{t_1}^{t_2} \partial T d\hat{t} = \frac{\rho A}{2}\int_{t_1}^{t_2} \partial\left[\int_0^L \left(\frac{\delta\hat{w}}{\delta t}\right)^2 d\hat{x}\right]d\hat{t} = \rho A\int_0^L\int_{t_1}^{t_2}\left[\frac{\delta\hat{w}}{\delta t}\left(\frac{\delta}{\delta t}\partial\hat{w}\right)\right]d\hat{t}\ d\hat{x},$$

$$= \rho A\left[\frac{\delta\hat{w}}{\delta t}\partial\hat{w}\right]_{t_1}^{t_2=t_2} - \rho A\int_0^L \frac{\partial^2\hat{w}}{\partial t^2}\partial\hat{w}d\hat{x} = -\rho A\int_0^L \frac{\partial^2\hat{w}}{\partial t^2}\partial\hat{w}d\hat{x} \qquad (2.21)$$

2.3.4 Non-conservative Work

The variation of non-conservative work done by external force can be expressed as:

$$\int_{t_1}^{t_2} \partial W_e d\hat{t} = \int_{t_1}^{t_2}\left(F(\hat{x},\hat{t})\partial\hat{w} - \hat{c}\dot{\hat{w}}\right)d\hat{t} \qquad (2.22)$$

where F is the transversely and uniformly distributed external applied force and $\hat{c}$ is the viscous damping coefficient. Substituting Equation (2.20-2.22) into the Hamilton Principle equation, Equation (2.19), and grouping the terms with coefficient " ∂u " we obtain:

$$\left(\hat{u}' + \frac{\hat{w}'}{2} + \hat{w}'\hat{w}_0'\right)' = 0 \qquad (2.23)$$

The elongation of the beam in the axial direction can be obtain by integrating Equation (2.23) over the beam length as follows:

$$\hat{u}(L,\hat{t}) - \hat{u}(0,\hat{t}) = \left(\hat{u}' + \frac{\hat{w}'}{2} + \hat{w}'\hat{w}'_0\right)L - \int_0^L \left(\hat{u}' + \frac{\hat{w}'}{2} + \hat{w}'\hat{w}'_0\right)d\hat{x} \qquad (2.24)$$

where, $\hat{u}(0,\hat{t})$ and $\hat{u}(L,\hat{t})$ denote the axial displacements of both boundaries $\hat{x}=0$ and $\hat{x}=L$ of the shallow arch beam. As shown in Figure 2.6, a fixed boundary condition at $\hat{x}=0$ is assumed while a compressive load N is assumed at the other boundary at $\hat{x}=L$. Therefore:

$$\begin{cases} \hat{u}(0,\hat{t}) = 0, \\ \hat{u}(L,\hat{t}) = -\dfrac{NL}{EA}, \end{cases} \qquad (2.25)$$

Substituting Equation (2.25) into Equation (2.24), we get:

$$\hat{u}' + \frac{\hat{w}'}{2} + \hat{w}'\hat{w}'_0 = \frac{1}{L}\int_0^L \left(\hat{u}' + \frac{\hat{w}'}{2} + \hat{w}'\hat{w}'_0\right)d\hat{x} - \frac{N}{EA} \qquad (2.26)$$

Subsequently, substituting Equations (2.20-2.22) in the Hamilton Principle Equation (2.19) and collecting the terms with coefficient "∂w" we get:

$$\rho A\ddot{\hat{w}} + EI\hat{w}'''' + \hat{c}\dot{\hat{w}} = EA\left(\hat{u}' + \frac{\hat{w}'}{2} + \hat{w}'\hat{w}'_0\right)'(\hat{w}'_0 + \hat{w}') + EA\left(\hat{u}' + \frac{\hat{w}'}{2} + \hat{w}'\hat{w}'_0\right)(\hat{w}''_0 + \hat{w}'') + F(\hat{x},\hat{t}) \quad (2.27)$$

Then, the nonlinear equation of motion of the shallow arch beam after substituting Equations (2.23-2.26) into Equation (2.27) we get:

$$\rho A\ddot{\hat{w}} + EI\hat{w}'''' + \hat{c}\dot{\hat{w}} = \left(\frac{EA}{2L}\int_0^L \left(\hat{w}'^2 + 2\hat{w}'\hat{w}'_0\right)d\hat{x} - N\right)(\hat{w}''_0 + \hat{w}'') + F(\hat{x},\hat{t}) \qquad (2.28)$$

To conclude, Equation (2.28) represents the displacement in the transverse direction for shallow arch beam displaced from its initial position that denoted by $\hat{w}_0(\hat{x})$ in Figure 2.2.

Chapter 3 : ARCHED BEAM STRUCTURAL RESPONSE USING REDUCED ORDER MODELING

In this chapter, we propose to derive the final form of equation of motion and their respective boundary condition of clamped-clamped arched microbeam. Then, the MEMS arch structural static and eigenvalue problems will be developed to compute its static deflection, natural frequencies and the corresponding modeshapes. We propose also to construct a Galerkin based reduced-order model and verify its integrity through comparison with experimental data and few ANSYS based finite-elements method simulations.

3.1 Equation of Motion

We consider a clamped-clamped curved microbeam of initial curvature $\hat{w}_0(\hat{x})$ and with dimension of the microbeam as described in Section 2.1. The initial elevation of the beam midpoint is d_0. The micro arch beam is exposed to half sine shock force at the midpoint of the arched beam along with electrostatic force of direct current only. The non-linear equation of motion of the arch assuming Euler-Bernoulli beam model for the transverse elevation $\hat{w}(\hat{x},\hat{t})$ is

$$EI \frac{\partial^4 \hat{w}}{\partial \hat{x}^4} + \rho A \frac{\partial^2 \hat{w}}{\partial \hat{t}^2} + \hat{c} \frac{\partial \hat{w}}{\partial \hat{t}} = F_{NL}(\hat{x}) + F_{EL}(\hat{x}) + F_{SH}(\hat{t}) \qquad (3.1)$$

where the mid-plane term, electrostatic and shock force is given by the following analytical expression:

$$F_{NL}(\hat{x}) = \left[\frac{EA}{2L}\left(\int_0^L \left(\left(\frac{\partial \hat{w}}{\partial \hat{x}}\right)^2 - 2\frac{\partial \hat{w}}{\partial \hat{x}}\frac{\partial \hat{w}_0}{\partial \hat{x}}\right)d\hat{x}\right) + \hat{N}\right]\left[\frac{\partial^2 \hat{w}}{\partial \hat{x}^2} - \frac{d^2 \hat{w}_0}{d\hat{x}^2}\right] \tag{3.2}$$

$$F_{EL}(\hat{x}) = \frac{\varepsilon_0 \, b \left(V_{DC}\right)^2}{2\left[d - (\hat{w}) + (\hat{w}_0)\right]^2} \tag{3.3}$$

$$F_{SH}(\hat{t}) = \hat{F}_{sh}\left[sin(\omega \hat{t})\,U(\hat{t}) + sin(\omega(\hat{t} - T_s))\,U(\hat{t} - T_s)\right] \tag{3.4}$$

Next and for convenience, we assume the following non-dimensional parameters:

$$w = \frac{\hat{w}}{d}; \quad w_0 = \frac{\hat{w}_0}{d}; \quad x = \frac{\hat{x}}{L}; \quad t = \frac{\hat{t}}{T}; \tag{3.5}$$

Substituting Equations (3.2-3.5) into Equation (3.1), we get:

$$\begin{aligned}
&EI\frac{\partial^4 (d\,w)}{\partial(L\,x)^4} + \rho A\frac{\partial^2 (d\,w)}{\partial(t\,T)^2} + \hat{c}\frac{\partial(d\,w)}{\partial(t\,T)} \\
&= \left[\frac{EA}{2L}\left(\int_0^L \left(\left(\frac{\partial(d\,w)}{\partial(L\,x)}\right)^2 - 2\frac{\partial(d\,w)}{\partial(L\,x)}\frac{\partial(d\,w_0)}{\partial(L\,x)}\right)d(L\,x)\right) + \hat{N}\right]\left[\frac{\partial^2 (d\,w)}{\partial(L\,x)^2} - \frac{d^2(d\,w_0)}{d(L\,x)^2}\right] + \\
&+ \hat{F}_{sh}\left[sin(\omega(t\,T))\,U(t\,T) + sin(\omega((t\,T) - T_s))\,U((t\,T) - T_s)\right] + \frac{\varepsilon_0 \, b \left(V_{DC}\right)^2}{2\left[d - (d\,w) + (d\,w_0)\right]^2}
\end{aligned} \tag{3.6}$$

Simplifying Equation (3.6), we get:

$$\begin{aligned}
&\frac{EI\,d}{L^4}w''' + \frac{\rho A L}{T^2}\ddot{w} + \frac{\hat{c}\,d}{T}\dot{w} = \left[\frac{EAL}{2}\int_0^1 \left((w')^2 - 2w'w_0'\right)dx + \hat{N}\right] \times \frac{1}{L}\left[w'' - w_0''\right] + \\
&+ \hat{F}\left[sin(\omega(t\,T))\,U(t\,T) + sin(\omega((t\,T) - T_s))\,U((t\,T) - T_s)\right] + \frac{\varepsilon_0 \, b \left(V_{DC}\right)^2}{2\,d^2\left[1 - (w) + (w_0)\right]^2}
\end{aligned} \tag{3.7}$$

where 'dots' denote derivatives with respect to time variable t and 'primes' denote derivatives with respect to space variable x. Next, multiplying Equation (3.7) by $L^4/EI\,d$ we get:

$$w'''' + \frac{\rho A L^4}{EI\,T^2}\ddot{w} + \frac{\hat{c}\,L^4}{EI\,T}\dot{w} = \frac{A\,d^2}{2\,I}\left[\int_0^1\left((w')^2 - 2w'w_0'\right)dx\right]\left[w'' - w_0''\right] + \frac{\hat{N}\,L^4}{EI\,d^2}\left[w'' - w_0''\right] +$$
$$+ \frac{\hat{F}_{sh}\,L^4}{EI\,d}\left[\,sin(\omega\,t\,T)\,U(t\,T) + sin(\omega((t\,T) - T_s))\,U((t\,T) - T_s)\right] +$$
$$+ \frac{L^4\,\varepsilon_0\,b}{2\,EI\,d^3}\frac{(V_{DC})^2}{[1 - w + w_0]^2}$$

(3.8)

Finally simplifying Equation (3.8), we get:

$$w'''' + \ddot{w} + c\dot{w} = \alpha_1\left[\int_0^1\left((w')^2 - 2w'w_0'\right)dx\right]\left[w'' - w_0''\right] + N\left[w'' - w_0''\right]$$
$$+ F\left[\,sin(\omega\,t\,T)\,U(t\,T) + sin(\omega((t\,T) - T_s))\,U((t\,T) - T_s)\right] + \alpha_2\frac{(V_{DC})^2}{[1 - w + w_0]^2}$$

(3.9)

while considering that $\frac{\rho A L^4}{T^2 EI} = 1$ and $w_0(x) = \frac{d_0}{2d}\left(1 - \cos(2\pi x)\right)$, and where the various non-dimensional parameters of Equation (3.9) are summarized in Table 3.1:

Table 3.1: Non-Dimensional Parameters for Parallel Plates Actuated Arch.

Time Constant:	$T = \sqrt{\dfrac{\rho A L^4}{EI}}$
Damping Parameter:	$c = \hat{c}\,\dfrac{L^4}{EI\,T}$
Stretching Parameter:	$\alpha_1 = \dfrac{A\,d^2}{2I} = \dfrac{b\,h\,d^2}{2\frac{1}{12}b\,h^3} = 6\left(\dfrac{d}{h}\right)^2$
Axial Force Parameter:	$N = \hat{N}\,\dfrac{L^4}{EI\,d^2}$
Shock Force Parameter:	$F = \hat{F}_{sh}\,\dfrac{L^3}{EI\,d}$
Excitation Frequency Parameter:	$\omega_f = \dfrac{\hat{\omega}_f}{T_s}$
Electric Force Parameter:	$\alpha_2 = \dfrac{L^4\,\varepsilon_0\,b}{2\,EI\,d^3} = \dfrac{L^4\,\varepsilon_0\,b}{2\frac{1}{12}b\,h^3 E\,d^3} = 6\,\dfrac{L^4\,\varepsilon_0}{h^3\,d^3\,E}$

3.2 Galerkin based Reduced-Order Modeling

The equation of motion of the shallow arch, Equation (3.9), is a nonlinear partial differential equation and therefore cannot be solved analytically. In the other hand, it can be solved numerically using a discretization technique such as the so-called Galerkin expansion method. This method will make things easy to obtain a reduced order model (ROM) [66]. Essentially, this technique would help to decuple a nonlinear partial differential equation (PDE) to a simplified ordinary differential equations (ODEs). This approach and all its details can be found in several nonlinear structural related books [1, 67].

The solution by separation of variables start by assuming the transverse response of the microbeam to be combination function in the following form:

$$w(x,t) = \sum_{i=1}^{n} u_i(t)\phi_i(x) \tag{3.10}$$

where, $\phi_i(x)$ represent the modeshapes functions of the clamped-clamped microbeam and $u_i(t)$ are its modal coordinates. The trail (admissible) functions for the clamped-clamped beam modeshapes are selected to be orthonormal functions so that:

$$\int_0^1 \phi_i(x)\phi_j(x)\,dx = \delta_{ij} = \begin{cases} 1 & i = j \\ 0 & i \neq j \end{cases} \tag{3.11}$$

In which (δ_{ij}) stands for the Kronecker delta operator. These modeshape equations are normalized if needed to satisfy the condition of Equation (3.10). Moreover, after further derivation we obtain [1]:

$$\int_0^1 \left(\phi_i(x)\,\phi''^{\,iv}_i(x) \right) dx = \omega^2_{non,i} \tag{3.12}$$

Next, multiply Equation (3.9) by $(1-w+w_0)^2$ to lower the numerical integration time [66, 68].

Then, by substituting Equation (3.10) into the resultant expression and multiply by $\phi_i(x)$ and integrating the outcome from 0 to 1, and keeping in mind the conditions of Equations (3.11) and Equation (3.12), we obtain ordinary differential equations in term of modal coordinates functions as follow [54]:

$$M_{ij}\ddot{u}_i(t) + C_{ij}\dot{u}_i(t) + K_{ij}u_i(t) = F_{EL} + F_{SH}(t) + \alpha_1\Gamma_i + N\int_0^1 \phi_i(x)[w'' - w_0''][1 - w + w_0]^2 dx \quad (3.13)$$

where:

$$M_{ij} = \int_0^1 \phi_i(x)\phi_j(x)[1 - w + w_0]^2 dx$$

$$C_{ij} = c\int_0^1 \phi_i(x)\phi_j(x)[1 - w + w_0]^2 dx$$

$$K_{ij} = \int_0^1 \phi_i(x)\phi_j^{iv}(x)[1 - w + w_0]^2 dx$$

$$F_{EL} = \alpha_2(V_{DC})^2 \int_0^1 \phi_i(x) dx$$

$$F_{SH}(t) = F\left[\sin(\omega\, t\, T)\, U(t\, T) + \sin(\omega((t\, T) - T_s))\, U((t\, T) - T_s)\right] \times$$
$$\int_0^1 \phi_i(x)\left[1 - \sum_{i=1}^n u_i(t)\phi_i(x) + w_0\right]^2 dx$$

And the nonlinear mid-plane term is given as follows:

$$\Gamma_i = \left[\int_0^1 \phi_i(x)[1 - w'' - w_0''] dx\right]\left[\int_0^1 \left(\left(\sum_{i=1}^n u_i(t)\phi'_i(x)\right)^2 - 2w'w_0'\right) dx\right] \quad (3.14)$$

As a special case for linear model the mid-plane terms are terminated by taking ($\Gamma_i = 0$) in Equation (3.14).

3.3 Eigenvalue Problem

In order to derive modeshapes of arched beam it requires finding the natural frequencies. These frequency can be obtained by solving the eigenvalue problem by assuming a solution of modeshapes in term of natural frequencies as follow:

$$w(x,t) = \phi(x)\, e^{j\omega_{non}\, t} \tag{3.15}$$

To get the linearized eigenvalue problem equation, we first linearize the equation of motion, Equation (3.13), set all damping and forcing terms equal to zero. The outcome of the linearized un-damped and un-forced equation is:

$$w'''' + \ddot{w} = \alpha_1\, w_0'' \left(\int_0^1 (2\, w'\, w_0')\, dx \right) \tag{3.16}$$

Substituting the function $w_0(x)$, Equation (3.15) into Equation (3.16), yields:

$$\phi^{iv} + \omega_{non}^2 \phi = 4\alpha_1 \pi^3 \left(\frac{d_0}{d} \right)^2 \cos(2\pi x) \int_0^1 \sin(2\pi x)\, \phi'(x)\, dx \tag{3.17}$$

Solution for Equation (3.17) consists of two parts, particular and homogenous solutions as follow:

$$\phi(x) = \phi_h(x) + \phi_p(x) \tag{3.18}$$

Next, by assuming the homogenous and particular solutions respectively as:

$$\phi_h(x) = A\, \cos(\sqrt{\omega_{non}}\, x) + B\, \sin(\sqrt{\omega_{non}}\, x) + C\, \cosh(\sqrt{\omega_{non}}\, x) + D\, \sinh(\sqrt{\omega_{non}}\, x)$$
$$\phi_p(x) = E\, \cos(2\pi x) \tag{3.19}$$

where *A, B, C, D* and *E* are constants.

Now, we substitute the particular solution into Equation (3.17) and solving will give the constant E [53]:

$$E = \frac{4\alpha_1\pi^3\left(\dfrac{d_0}{d}\right)^2 \displaystyle\int_0^1 \sin(2\pi x)\phi'_h(x)\, dx}{16\pi^4 - \omega^2_{non} + 4\alpha_1\pi^4\left(\dfrac{d_0}{d}\right)^2} \tag{3.20}$$

It's clear that the constant E depend on the constants A, B, C and D, which can be determined by applying following boundary conditions of a clamped-clamped microbeam after normalization.

$$w(0,t) = 0 \,;\ \frac{\partial w}{\partial x}(0,t) = 0 \,;\ w(1,t) = 0 \,;\ \frac{\partial w}{\partial x}(1,t) = 0 \,; \tag{3.21}$$

Now, to examine the change of the natural frequencies and modeshapes of the arch microbeam with various non dimensional rise levels. We introduce new parameter d_{non} to represent the non dimensional initial rise as [53, 69]:

$$d_{non} = \frac{2\sqrt{3}\, d_0}{h} \tag{3.22}$$

where, d_0 and h are mid-point initial rise and thickness in micro meters respectively.

Substituting Equations (3.22) into Equations (3.20) and the resultant with Equation (3.21) into Equation (3.18) will result into five algebraic equations that can be re-written into the following matrix form [69]:

29

$$\begin{pmatrix} 1 & 0 & cos(\omega_{non}^{1/2}) & -sin(\omega_{non}^{1/2}) & -\dfrac{4\,\pi^4\,d_{non}^2\,\omega_{non}^{1/2}\,sin(\omega_{non}^{1/2})}{4\,\pi^4-\omega_{non}} \\[3mm] 0 & 1 & sin(\omega_{non}^{1/2}) & cos(\omega_{non}^{1/2}) & \dfrac{4\,\pi^4\,d_{non}^2\,\omega_{non}^{1/2}\,cos(\omega_{non}^{1/2})}{4\,\pi^4-\omega_{non}}-\dfrac{4\,\pi^4\,d_{non}^2\,\omega_{non}^{1/2}}{4\,\pi^4-\omega_{non}} \\[3mm] 1 & 0 & cosh(\omega_{non}^{1/2}) & sinh(\omega_{non}^{1/2}) & \dfrac{4\,\pi^4\,d_{non}^2\,\omega_{non}^{1/2}\,sinh(\omega_{non}^{1/2})}{4\,\pi^4+\omega_{non}} \\[3mm] 0 & 1 & sinh(\omega_{non}^{1/2}) & cosh(\omega_{non}^{1/2}) & \dfrac{4\,\pi^4\,d_{non}^2\,\omega_{non}^{1/2}\,cosh(\omega_{non}^{1/2})}{4\,\pi^4-\omega_{non}}-\dfrac{4\,\pi^4\,d_{non}^2\,\omega_{non}^{1/2}}{4\,\pi^4+\omega_{non}} \\[3mm] 1 & 0 & 1 & 0 & 16\,\pi^4+2\,\pi^4\,d_{non}^2-\omega_{non}^2 \end{pmatrix} \begin{Bmatrix} A \\ B \\ C \\ D \\ E \end{Bmatrix} = \begin{Bmatrix} 0 \\ 0 \\ 0 \\ 0 \\ 0 \end{Bmatrix} \quad (3.23)$$

In order to find a non-trivial solution for the above equation, the determinant of the matrix in Equation (3.23) should be equated to zero. This yields the following nonlinear equation function of the shallow arch natural frequencies (the characteristic equation):

$$\frac{2}{16\,\pi^4-\omega_{non}^2}[256\pi^8+32\pi^8 d_{non}^2-32\pi^4\,\omega_{non}^2-2\pi^4\,d_{non}^2\,\omega_{non}^2+8\pi^4\,d_{non}^2\,\omega_{non}^{3/2}\,sin(\omega_{non}^{1/2})+$$
$$-cosh(\omega_{non}^{1/2})(cos(\omega_{non}^{1/2})(16\,\pi^4-\omega_{non}^2)(2\,\pi^4(8+d_{non}^2)-\omega_{non}^2)+8\,\pi^4\,d_{non}^2\,\omega_{non}^{3/2}\,sin(\omega_{non}^{1/2}))+ \quad (3.24)$$
$$+16\,\pi^4\,d_{non}^2\,\omega_{non}^{3/2}\,sin(\omega_{non}^{1/2}/2)^2\,sinh(\omega_{non}^{1/2})+\omega_{non}^4]=0$$

The above equation is a multi-valued nonlinear equation function of the non-dimensional frequency, therefore it should be numerically solved with initial guesses for every assumed initial rise. Then, after acquiring each frequency as function of the beam initial rise, we can substitute its value into Equation (3.23), to solve for the five constants of integration *A, B, C, D* and *E*, to get the corresponding modeshapes expression using Equation (3.18).

It is worth mentioning that the obtained modeshapes expressions and their respective non-dimensional frequencies are valid for the case of straight beams when assuming $d_0=0$ which results into a zero particular solution, i.e. $E=0$, and a non-zero homogenous solution depicting the modeshapes of straight beams [70].

3.4 Shallow Arch Natural Frequencies and Modeshapes

In this section, we propose to derive mathematical expressions of the modes shapes of a straight clamped-camped beam by setting $w_0(x) = 0$ in Equation (3.16) and assuming solution of homogenous type. To this end, solving Equation (3.24) for the first four modes yields modeshape equations in form of [1]:

$$\phi_i(x) = \left[\cosh(\sqrt{\omega_{non,i}}\, x) - \cos(\sqrt{\omega_{non,i}}\, x)\right] - \sigma_i \left[\sinh(\sqrt{\omega_{non,i}}\, x) - \sin(\sqrt{\omega_{non,i}}\, x)\right] \quad (3.25)$$

where, Table 3.2 represent the corresponding normalized frequencies and constant of integrations in Equation (3.25).

Table 3.2: Respective modeshape normalized frequencies ω_{non} and its respective constant of integration σ_i.

Mode	$i=1$	$i=2$	$i=3$	$i=4$
$\omega_{non,i}$	22.3733	61.6728	120.9033	199.8594
σ_i	0.98250	1.00078	0.99997	1

Plotting Equation (3.25) for the first four mode-shapes we get the following plots:
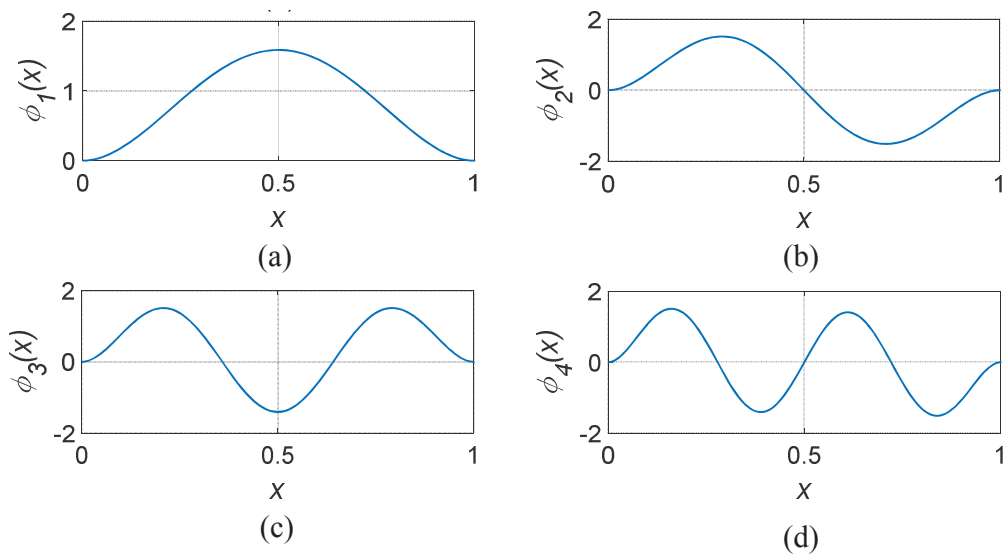
Figure 3.1: (a) First (b) Second (c) Third (d) Fourth modeshapes of a straight clamped-clamped microbeam.

31

Solving Equation (3.24) at different values of d_{non} and plotting the resultant first modeshape, Figure 3.2. We can conclude that as we increases the initial rise the first modeshape tend to deviate from the straight beam modeshape.
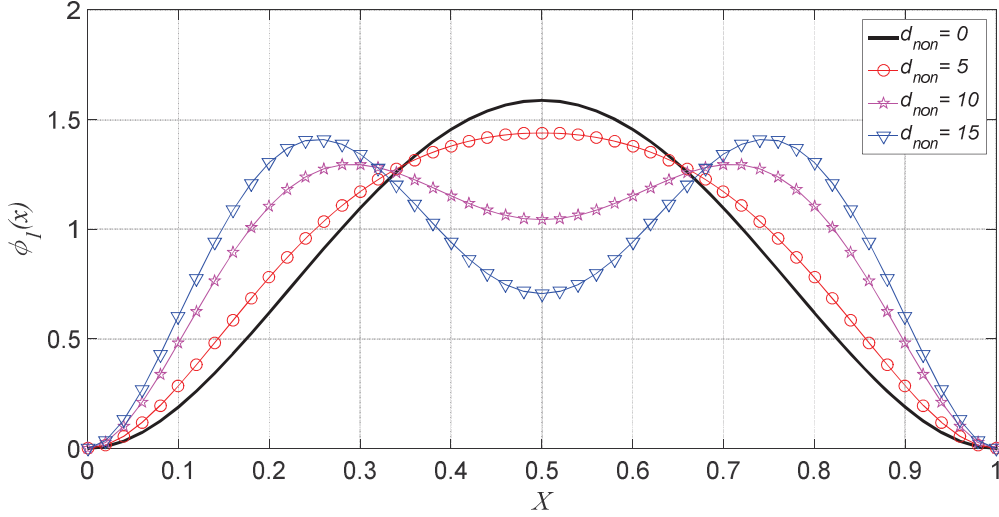
Figure 3.2: First arch modeshape as function of its normalized initial rise level.

Figure 3.3 represent the first five natural frequencies as the initial rise change. Moreover, it appears that there is multiple crossing between odd and even natural frequencies. This can lead to internal resonances [59]. Furthermore, even frequencies are constant for all the value of rise.
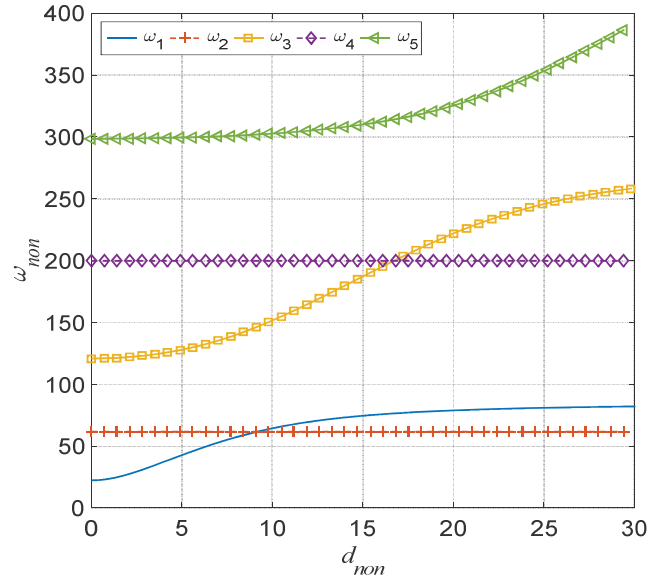
Figure 3.3: Variation of the shallow arch first five natural frequencies as function of its normalized initial rise.

The following table summarizes first, second, third, fourth and fifth modes shape for varying d_{non} :

Table 3.3: The shallow arch simulated first five modeshapes as function of its normalized initial rise.

3.5 Code Validation

In this section, we will use Equation (3.13) to derive un-coupled ODEs in order to investigate the dynamic responses of a straight microbeam under different mechanical shock loads with profiles of half sine, unit-step and saw-tooth with varying amplitude and durations. First, the outcome will be compared to previously published results. The second comparison will be conducted using electrostatic force for a shallow arched microbeam. Lastly, the combined effect of shock and electrostatic forces will be verified with previously published experimental data along with an ANSYS based finite element simulations.

3.5.1 Dynamic Response of Straight Microbeams under Mechanical Shock Loads

The response of a mechanical system to mechanical shock can be determined through various ways: a shock response spectrum (frequency domain approach: where the steady-state maximum response of the system is determined function of a given shock duration), or a time history of the system (time domain approach: by plotting the dynamic response of the structure function of time which represent its transient and steady state dynamic responses). We propose formerly to use both approaches in order to compare with previously published results and to perform a parametric study on the effect of the mechanical shock load shape, amplitude and duration on its shock spectrum as well as on its dynamical response. In this regards, we propose to use Equation (3.13) and solve it with respect to time. Assuming the material properties of the considered microbeam are summarized in Table 3.4:

Table 3.4: Extracted straight microbeam geometrical and material properties used for ROM verification [72].

Length (L)	900 μm	Width (b)	100 μm
Thickness (h)	1.5 μm	Initial rise (d_0)	0 μm
Young's Modulus (E)	169 GPa	Density (ρ)	2332 kg/m^3

The non-linear ODEs equations are numerically solved using a numerical tool in Mathematica® [71] software. First, we compare our numerical simulations of a straight beam under a half sine response to previously published results [72]. Figure 3.4 displays the time history of the normalized maximum deflection of the straight beam under the effect shock amplitude of 1000g half sine shockwave for two distinct shock durations. The blue circled solid line are the results from [72], and black solid line represent the results of this investigation. We can see from the figure that the comparison is showing an excellent agreement and hence validating our numerical code.

Figure 3.5 shows the variation of the normalized maximum response of the straight beam with different shock amplitudes graph and for a shock durations of 1ms and 0.1ms as follow. We can clearly see from figure 3.5 that for small amount of shock amplitudes, the response is nearly linear and then switch to be nonlinear for higher amplitudes. This is obvious since we are considering here a nonlinear beam model (with mid-plane stretching term) undergoing nonlinear behavior for higher deflections.

(a)   (b)
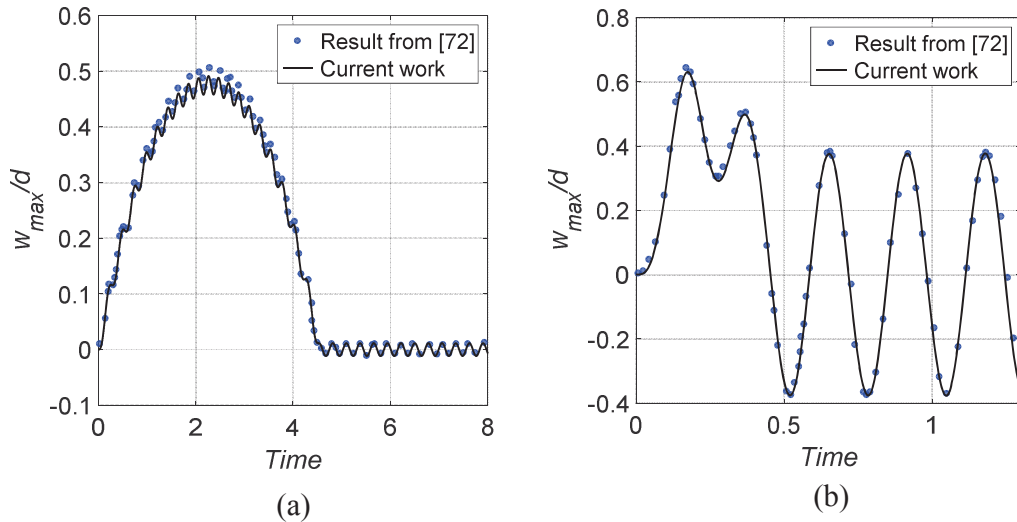
Figure 3.4: Half sine wave response assuming 1000g amplitude and two shock durations of (a) 1 ms and (b) 0.1 ms.

35
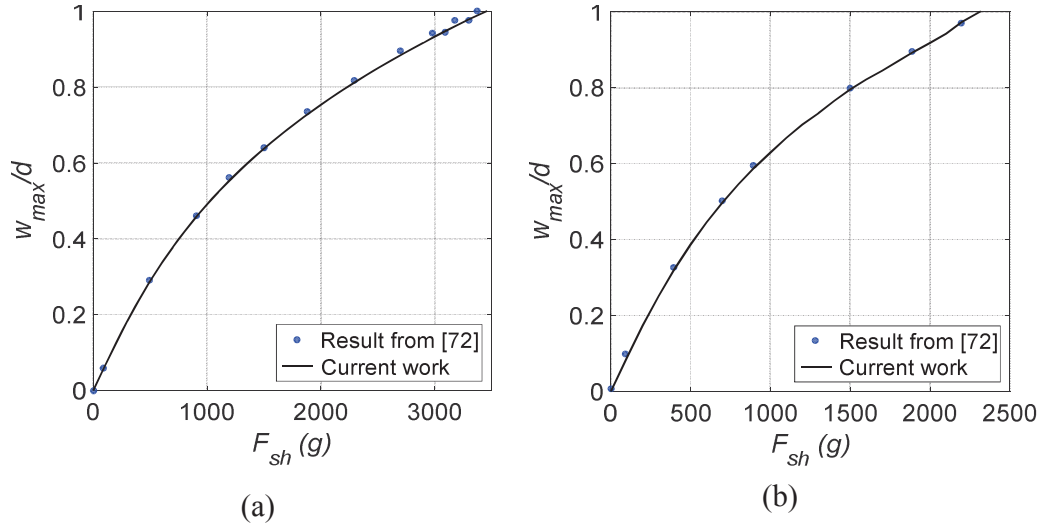
Figure 3.5: Straight normalized microbeam's maximum response values vs. the shock amplitude for two shock durations of (a) 1 *ms* and (b) 0.1 *ms*.

In the results of both Figures 3.1 and 3.2, we assumed a non-damped system. In the following results, we propose to add damping to the system through a damping ratio of 0.1. Figures 3.6 and 3.7 represent the straight beam dynamic response under both unit-step and saw-teeth respectively. And assuming a shock amplitude of 1,000g and a shock duration of 1ms.
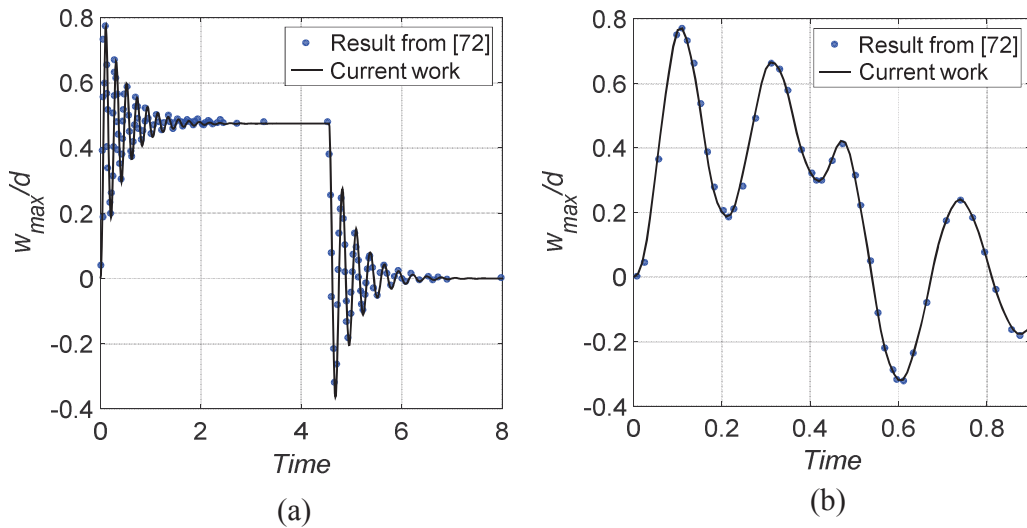
Figure 3.6: The unit step wave response for 1000g amplitude and assuming two shock durations of (a) 1 *ms* and (b) 0.1 *ms*.

36

From the unit-step response of Figure 3.6, we can comprehend that the beam settling time is proportional to the shock duration. It can also be noted that in case of 1ms shock duration there is an initiation of two disturbances: the first due to a sudden increase in the shock amplitude and the second is due to sudden decrease in the shock amplitude.

(a)   (b)
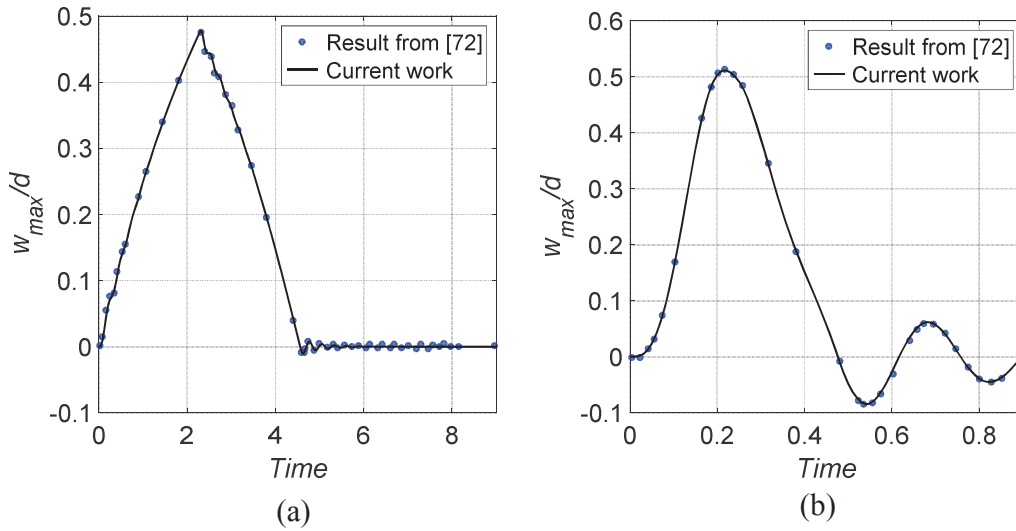
Figure 3.7: The saw-tooth wave response at 1,000g amplitude and assuming two shock durations of (a) 1 ms and (b) 0.1 ms.

3.5.2 Static Response of Arched Beam Under Electro-static Force

In addition, the code will be verified with experimental results represented in [73] under electrostatic force only. The code uses four odd (symmetric) arched and straight modeshapes for simulation. Unless stated otherwise, the following assumed material properties given in Table 3.5 will be used throughout this work. Later, we will study the effect of numbers of assumed modes and the difference between both straight and arched modes in the upcoming subsection.

Table 3.5: Assumed shallow micro-arch MEMS geometrical and material properties for ROM validation.

Length (L)	1000 μm	Width (b)	30 μm
Thickness (h)	2.4 μm	Initial rise (d_0)	3 μm
Young's Modulus (E)	166 GPa	Density (ρ)	2332 kg/m^3

37

Figure 3.8 represents the experimental results from [73] represented by black dots, blue triangles are the simulated data using four arched modeshapes and red circles are the simulated data using four straight modeshapes. We can see clearly an acceptable match between all the data and thus validating the numerical code with DC voltages applied on the structure.
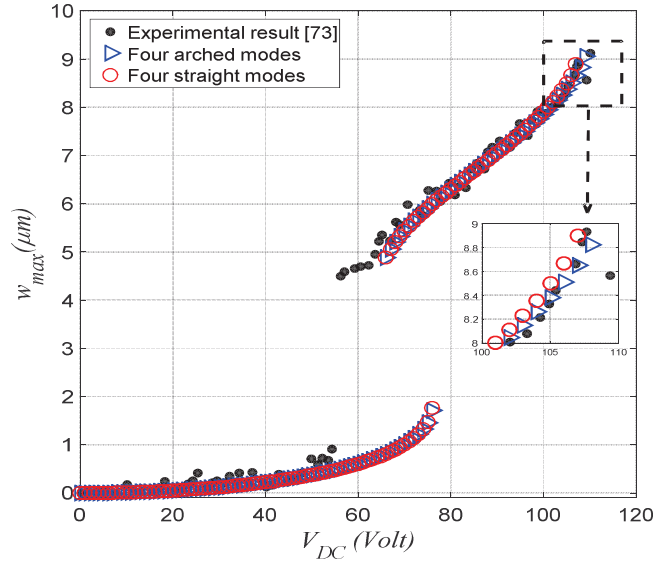
Figure 3.8: Comparison between the ROM results while considering both straight beam and arched beam odeshapes in the Galerkin decompsoition with published experimental data of the maximum static deflection of a shallow arch under various DC voltages.

3.5.3 Response of Arched Beam under Combined Loading

Further verification to the code will be conducted by comparing it with the ANSYS®[74] Finites Element Method (FEM) simulations under combined loading of half sine shock wave and a DC electrostatic load. We used for this comparison the geometrical and material properties of the shallow arch of Table 3.5, a DC load of 50 *Volt*, a damping ratio of 0.5 along with four modeshapes in the ROM.

Figure 3.9 shows the implemented ANSYS based FEM model consisting of two nodes TRANS126 element: one is assumed for the electrical potential deference and the second is for

the structural degree of freedom. Which was assumed as the element in ANSYS. This TRANS126 element is mainly used as a good candidate for problem involving electrostatic-structural coupling. The attractive force caused by the voltage deference across the element is resisted by the stiffness of the microbeam with both ends fixed.

After running several FEM simulations for various shock amplitudes, we plot the shallow arch maximum dynamic response considering two shock durations of 20 millisecond (represented by cross symbols) and 100 millisecond (represented by dots) respectively in Figure 3.10. In the same figure, ROM simulations are also shown by diamonds and circles for the shock duration of 20 and 100 millisecond respectively. It's clear that both sets of produced results matching with these from ANSYS. The shock spectrum was also generated in Figure 3.11, using both FEM and ROM simulations when assuming zero damping, shallow arch length of 500 μm, initial rise of 10 μm and a shock amplitude of 1,000g, and both numerical approaches are showing an excellent agreement.
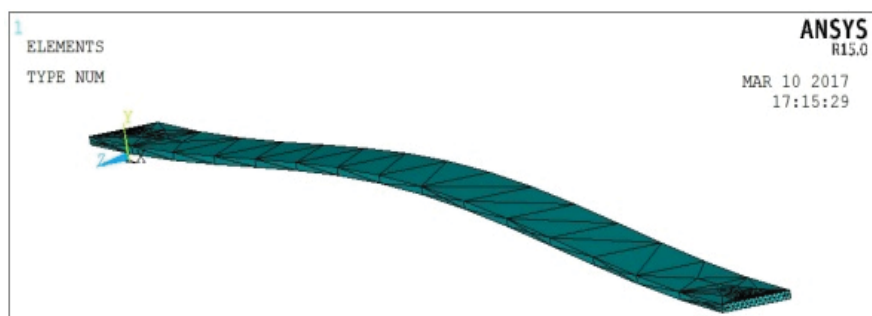
Figure 3.9: ANSYS model of clamped-clamped shallow arch microbeam.
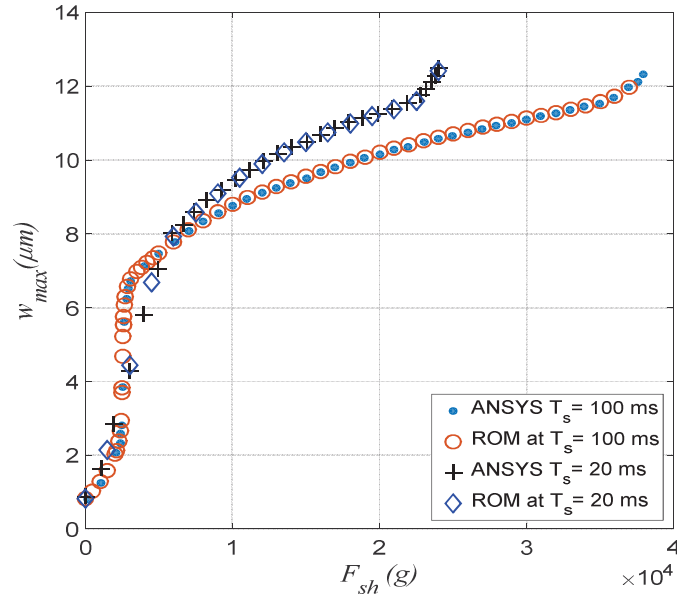
Figure 3.10: Comparison between the ROM and FEM-ANSYS results showing the variation of the shallow arch mid-point defclection with the shock load amplitude, for $V_{DC} = 50$ *Volt*, and for two shock durations of 20 and 100 *ms*, respectively.
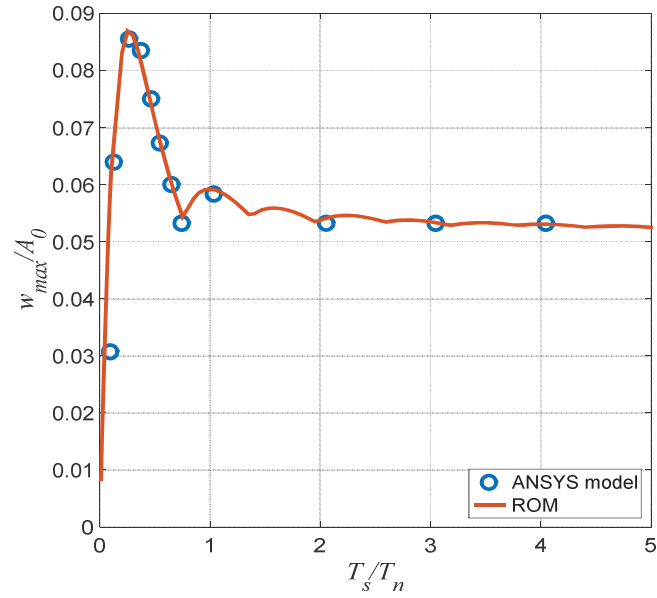
Figure 3.11: Comparison between the ROM and FEM-ANSYS results showing the variation of the shock spectrum under 1,000-*g*'s shock amplitude and zero damping ratio.

3.6 Reduced Order Model Convergence Analysis

In this section we will investigate the reduced-order modeling when assuming straight and then arched modeshapes in the modal Galerkin decomposition. Moreover, we will examine the influence of including the even (ant-symmetric) and odd (symmetric) modeshapes in the ROM process. Finally, we will study the needed number of modes to ascertain the convergence of the ROM numerical results.

3.6.1 Assuming Straight and Arched Beam Modeshapes

Re-calling Equation (3.19) we can see that the difference between straight and arched modeshape is the constant E. Where this constant is equal to zero in case of straight modeshapes, while in arched modeshape it's different than zero [70]. Now, considering the following case study of microbeam response under mechanical shock of amplitude of $6500g$ and $16500g$ which represent the case of without/with snap-through respectively for shock duration of 0.4 T_n and 4 T_n to represent dynamic and quasi-static ranges. It's clear from both Figure 3.12 and Figure 3.13 that using six arched (circles) or six straight (solid line) modeshape will lead to the same result in any combined case of snap-through or without snap-through and dynamic or quasi-static ranges. Thus, in the upcoming results, we will assume arched modes as basic functions in simulating the ROM equations.
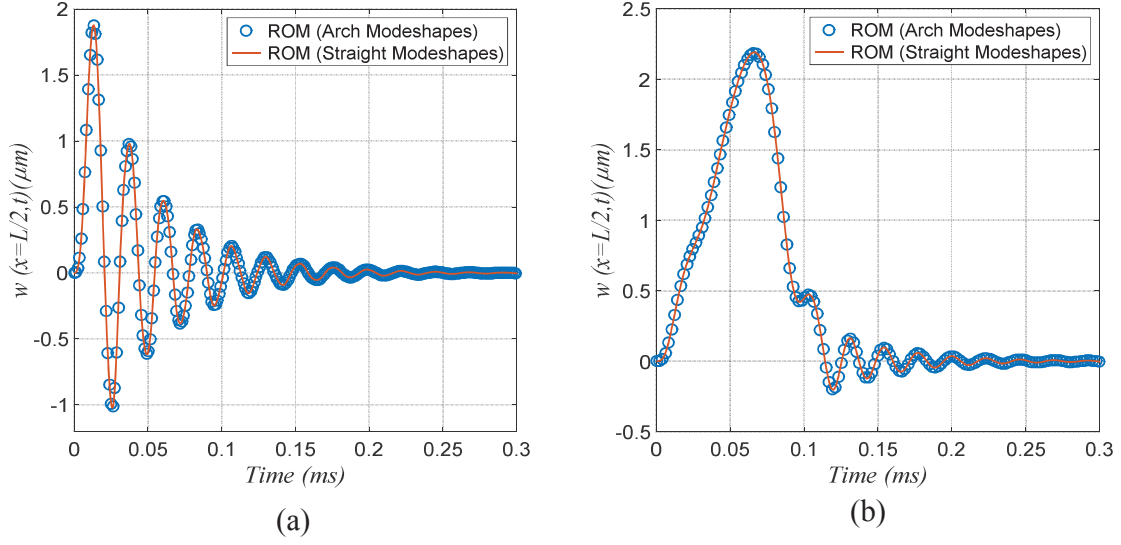
Figure 3.12: Beam responce under half sine shock of amplitude 6500*g* (a) Dynamic range (b) Quasi-static range.
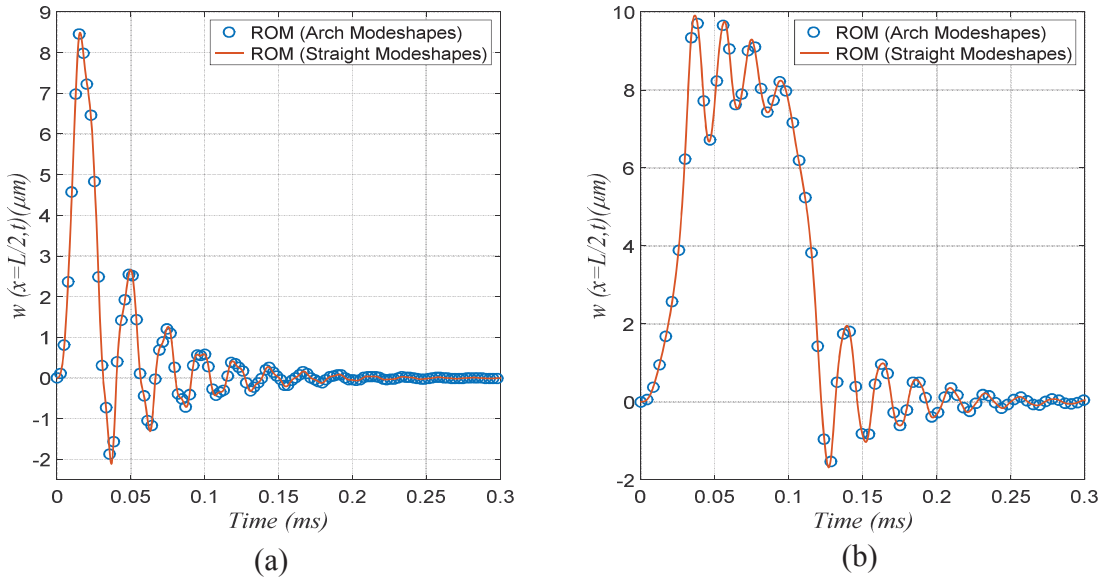
Figure 3.13: Beam response under half sine shock of amplitude 16500*g* (a) Dynamic range (b) Quasi-static range.

3.6.2 Even Modeshapes Effects

In this section we will study if even modeshape is playing a significant role, or can it be neglected and consider only the odd number of modeshape in the assumption of Equation (3.19). Considering the following case study of clamped-clamped microbeam at *x=L/2* under V_{DC}= 30 *Volt* and half sine shock with varying amplitude with two shock duration 0.4 T_n and 4 T_n, in both

Figures 3.14-(a) and (b), while T_n is the micro-arch first natural period evaluated in this case as 0.0284 *ms*. In the onset of each figure, we show two time responses of the shallow arch to the mechanical shock pulse at two different amplitudes 6500*g* and 16500*g*, respectively, and for both duration $0.4T_n$ and $4T_n$.

It can be seen that the shallow arch experiences the shock pulse as a quasi-static load, i.e. the time response looks similar to the shock wave pulse, for the case of $T_s = 4T_n$, however it experiences the same wave as a dynamic load, for the case of $T_s = 0.4T_n$. This is mainly because the first natural period of the shallow arch is much smaller than the shock wave duration in the quasi-static case and close to the shock pulse duration for the other dynamic load case. It can also be noticed from both figures that the maximum deflection of the micro-arch in the case of quasi-static is larger than that one in the dynamic case. The first case is showing a sudden dynamic snap-through motion whereas the second is showing a completely different behavior where the snap-through motion is not happening suddenly but in a more continuous manner. These sensitivity of the structural behavior of MEMS arches to the shock profiles has to be taken into account when assuming them in MEMS devices. A final conclusion about this figure that the results when considering even modes in constructing the ROM equations are perfectly coinciding with those when odd modes are involved. Hence, even modes have lower effect on the ROM solutions as compared to odd modes. To insure this results, relative error will be calculated in Table 3.6 for both shock duration cases at $F_{sh} = 18{,}000g$ throw the following equation:

$$RE_i = \frac{R_i - R_{i+1}}{R_i} \times 100$$

(3.26)

where, RE is relative error and R_i is the response value using ROM i^{th} mode.
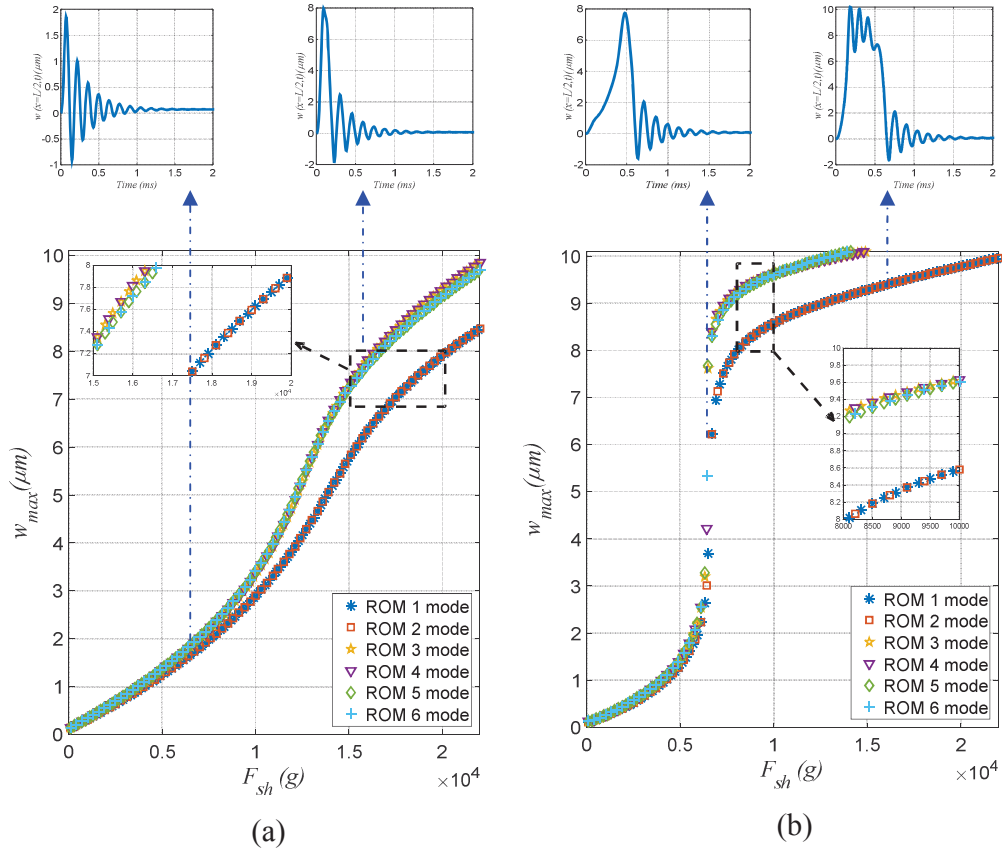
Figure 3.14: Beam response vs. shock amplitude and V_{DC}=30 *Volt* at shock duration (a) 0.4 T_n and (b) 4 T_n.

Table 3.6: Relative error comparison between the assumed ROM number of modes for two shock durations (a) 0.4 T_n and (b) 4 T_n.

(a)		(b)	
Reference i^{th} mode	Relative Error (%)	Reference i^{th} mode	Relative Error (%)
1	2.2×10^{-4}	1	1.1×10^{-4}
2	2.43	2	4.22
3	3.6×10^{-6}	3	6.3×10^{-6}
4	1.03	4	1.40
5	6.9×10^{-6}	5	3.2×10^{-6}

It appears from the Table 3.6 that the relative error for even modeshapes are zero. To further investigate this latter observation, we propose to plot the maximum values of the first six ROM modal coordinates u_1-u_6 using a log-log scale in Figure 3.15. It's again clear from the

44

figure that even modes has the low contribution in the all assumed shock amplitudes and for both assumed shock durations, Figures 3.15-(a) and (b). This figure can also illuminate on the contribution of the lower and higher-order modes in the overall dynamic response of shallow arches. For example, when comparing Figure 3.15-(a), where the response is dynamic, to Figure 3.15-(b), where the response is quasi-static, we can clearly see that all odd frequencies seem to participate and only the fundamental first mode seem to be responsible of the sudden initiation of the snap-through motion (see red circle in Figure 3.15-(b)). Therefore, neglecting the odd higher order terms in the Galerkin expansion in such cases may affect the accuracy of the predicted behavior, and consequently, from now on, only odd modeshape will be considered in simulating the ROM results in the coming sections.
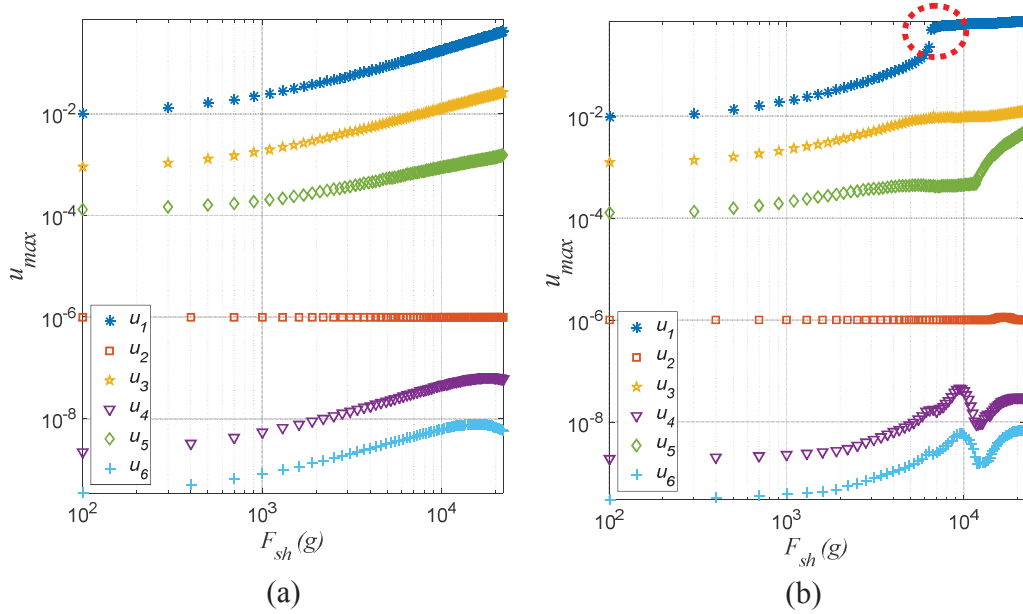
Figure 3.15: Comparison of the six modal ROM coordniates for shock duration (a) 0.4 T_n and (b) 4 T_n.

In Figure 3.16, we propose to investigate the effect of changing where to evaluate the shallow arch dynamic response trough considering different beam span positions as follows: $x= L/4$, $L/3$ and $L/2$. We can conclude from the figure that the even modes are still obsolete in

contributing in the calculation of the maximum dynamic response of the shallow arch at different beam span positions. The only change can be noticed is the beam maximum deflection amplitude, but the main trend is approximately common at any beam span positions.
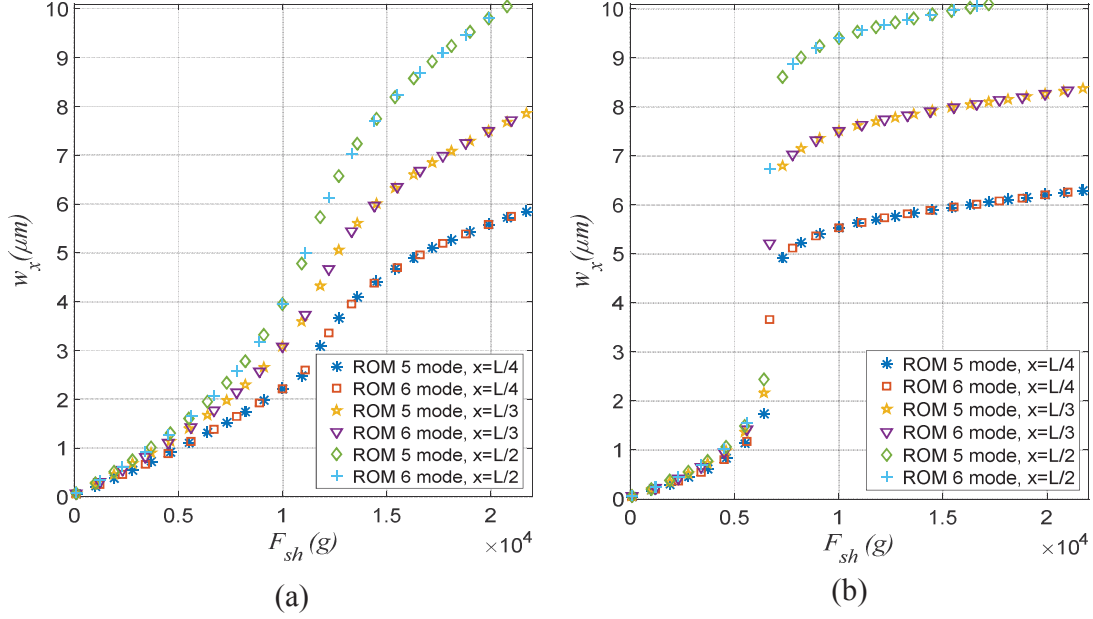
Figure 3.16: Beam response vs. shock amplitude and V_{DC}=20 $Volt$ at $x = L/4$, $L/3$ and $L/2$ for shock duration of (a) 0.4 T_n and (b) 4 T_n.

3.6.3 Number of Assumed Modes in the Galerkin Decomposition

Investigating the required number of modes needed in the Galerkin decomposition for convergence of the ROM multi-modes results. As previously admitted in numerous previous investigations such as [1], in such modal decomposition approach, a single mode assumption cannot accurately capture the dynamic behavior of continuous systems. Therefore, we display the variation of the maximum mid-point shallow arch static deflection with the DC load in Figure 3.17, while considering 1 up to 6 odd modes in the Galerkin decomposition. The figure shows that when considering only one mode the pull-in voltage is around ≈95$Volt$, whereas when

increasing to six modes, the pull-in voltage converged to a value of $\approx107\,Volt$. Using Equation (3.26) to show the variation of the relative error in the calculation of the pull-in voltage for various number considered modes in the ROM process is demonstrated in Table 3.7. The results of the table shows that retaining only 4 modes in the ROM process is enough to capture the dynamical response of the shallow arch within an acceptable error of $\approx3\%$. In addition, Figure 3.17 is demonstrating that this bi-stable system structural response can be categorized into three main comportments: For low DC voltages, the system is deflecting around its initial shape. Then for some DC voltage values greater than a certain threshold, the system is undergoing a hysteretic type of behavior showing bi-stable states where the shallow arch can deflect around its natural shape, or around its symmetric inverted shape, or in moving in large deflection between. Finally for higher DC loads that are below the pull-in voltage onset, the system is gaining again a mono-stability regime by bending around only the inverted symmetric shape.
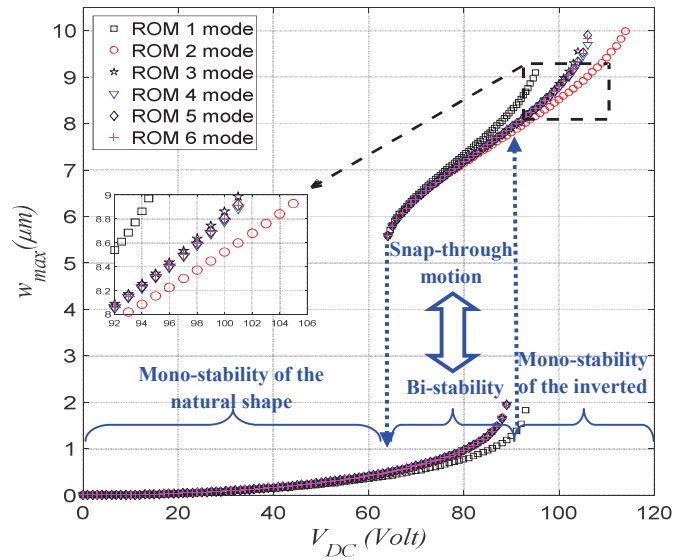
Figure 3.17: Shallow arch maximum static deflection versus the DC voltage assuming up to six symmetric modeshapes in the ROM based Galerkin decomposition.

Table 3.7: Relative error calculation of the pull-in voltage calculations while assuming different modes in the ROM at V_{DC}= 95 *Volt*

Reference ith mode	Relative Error (%)
1	11.62
2	2.28
3	0.42
4	0.13
5	0.03

Thus, in the upcoming chapters four odd arched modeshapes will be adopted in the assumed solution for analyzing the considered problem.

Chapter 4 : ARCH RESPONSE UNDER MECHANICAL SHOCK WAVES AND ELECTRIC LOADS INDEPENDENTLY

In this chapter, the effect of the initial rise is studied in shallow arched microbeam under pure mechanical shock then under V_{DC} load only. Response, shock spectrum and deflection vs. shock amplitude will be established for various initial rise values. Unless stated otherwise, four symmetric (odd) arched modeshapes will be used at $x=L/2$ with defaults microbeam material properties (Table 3.5) with damping ratio of 0.1 and initial rise $d_0 = 4 \ \mu m$.

4.1 Response Under Mechanical Shock Loads Only

Mechanical shock load can affect the microbeams in dynamic or quasi-static depending on the natural period of the forcing. In case of dynamic behavior, the response will be amplified as the shock period reaches or near the natural frequency of the structure. As the shock period increases beyond natural frequency of the system, the response will act as in quasi-static behavior. Figure 4.1 shows the difference between the two behaviors in case of snap-through and without snap for different shock durations.
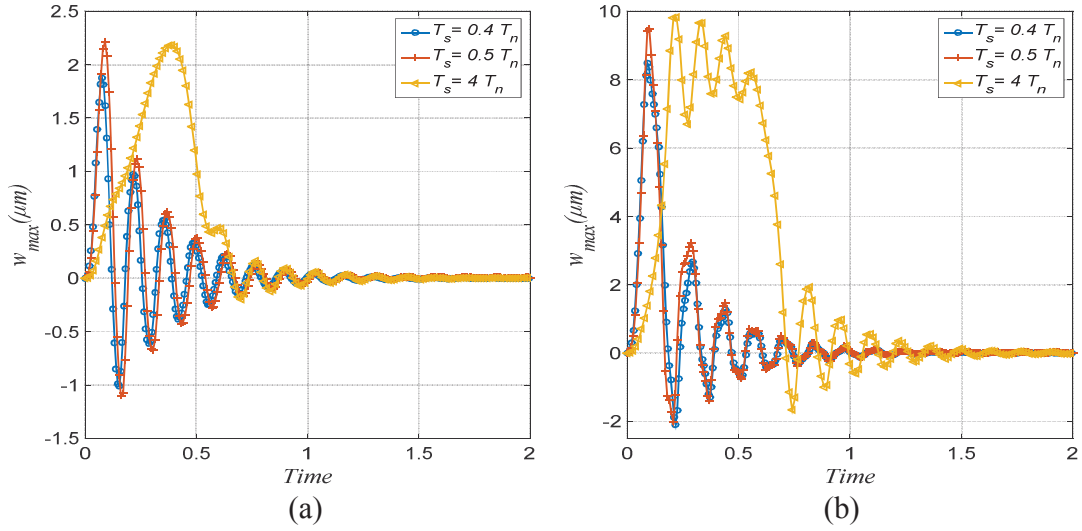
Figure 4.1: Time response for different shock period under pure half sine shock load (a) without snap-through (b) with snap-though.

4.1.1.1 Effect of Initial Rise on Force Response

Next, we propose to investigate the variation of the shallow arch of Table 3.5 maximum dynamic displacement while varying the shock wave amplitude and assuming two different shock durations, Figures 4.2-(a) and (b). To better understand the shallow arch different nonlinear structural scenarios under the effect of shaking environment only, we assumed in the same comparing figure four different values of the its initial rise. Moreover, since in almost all the subsequent simulations we will assume different values of DC load and micro-arch initial rises, and as we will undertake variation of the shock wave durations as function of the shallow arch natural periods, Table 4.1 summarizes all the considered shallow natural period cases.

Table 4.1: The calculated natural periods (in *ms*) of all considered below case studies of the micro-arch initial rise and respective DC loading conditions.

	V_{DC}=0 *Volt*	V_{DC}=30 *Volt*	V_{DC}=60 *Volt*	V_{DC}=90 *Volt*
d_0= 0 *µm*	0.048	0.0475	0.035	0.0261
d_0 =2 *µm*	0.0344	0.038	0.0883	0.0283
d_0 =3 *µm*	0.0278	0.0292	0.0365	0.0276
d_0 =4 *µm*	0.0235	0.0241	0.0265	0.036

It follows from Figure 4.2 that the initiation of the dynamic snap-through motion is totally

50

different when we considered lower shock duration and then a higher value. The arch showed, for the case of $T_s=0.4T_n$ and for all assumed values of its initial rise, only one continuous solution for the entire range of shock loading amplitudes and therefore suppressing any abrupt bi-stability hysteretic possibility, Figure 4.2-(a). This behavior is mainly attributed to the fact that the arch is recognizing the shaking wave as a dynamic load and then the beam would not have any stationary process to initiate an immediate snap-through motion. On the other hand, for the case of $T_s=4T_n$ and for non-zero initial rises, the bi-stable system experienced an abrupt change in its maximum dynamic deflection from lower value to higher value at certain shock loads thus illustrating a dynamic bi-stable behavior, Figure 4.2-(b). The main reason of this different comportment is that the arch is identifying here the shaking wave as a quasi-static load and then the beam would have two discontinuous behavior and offering the possibility of a two stable switch states. In this latter case, we can also understand from Figure 4.2-(b) that if we increase the arch initial rise, i.e, increase its natural frequency and therefore decrease its natural period, the bi-stable regime become more noticeable and the system would have more clear stable dual states.
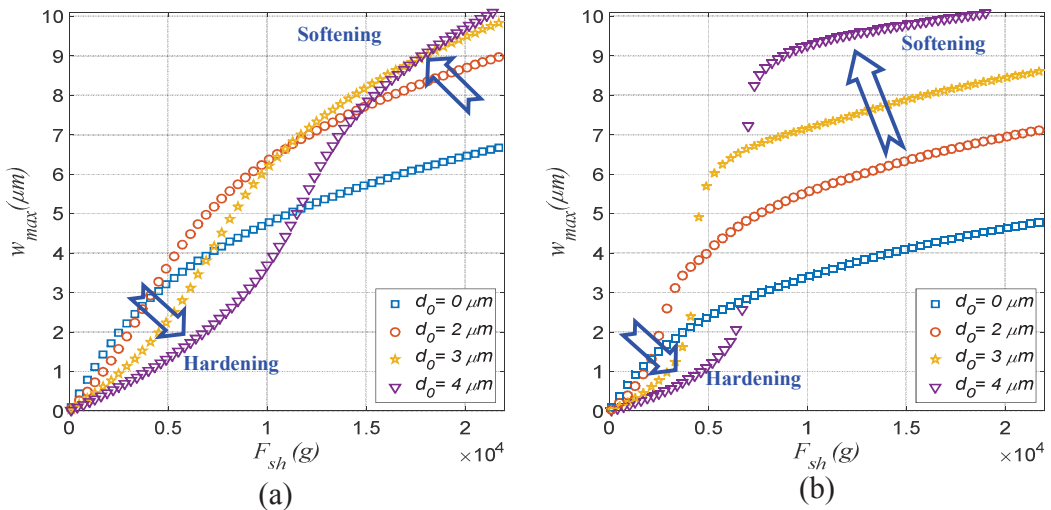
Figure 4.2: Variation of the shallow arch maximum dynamic response with the shock load amplitude considering different beam initial rise, with zero DC load, and for two different shock durations of (a) $0.4T_n$ (b) $4T_n$.

51

Furthermore, another interesting structural comportment one can comprehend from the above figures that as the arch initial rise value increase, the shallow arch maximum dynamic deflection shows its nonlinear relationship with the shock loads changing from being of hardening type (curve concave down) to a softening type (curve concave up). This is mainly due to the fact that there is two main nonlinear components competing in this problem: the geometric mid-plane stretching nonlinearity which is mostly of a hardening nature and the geometric initial curvature nonlinearity which is essentially of a softening nature. We can also understand that this behavior is totally different before and after the initial of the snap-through instability as shown in the onset of both Figures 4.2-(a) and (b).

4.1.1.2 Effect of Damping

Next, It's well known that damping ratio is one of the important factors in microbeams behaviors. Thus, in this part we will investigate the effects of damping on microbeam response for both dynamic and quasi-static behaviors. Figure 4.3 shows the maximum deflection as shock amplitude varying for several damping ratios. We can notice that increasing the damping of a system will result in delay the snap-through point if there is any. Also, it will allow us to operate the system beyond pull-in voltage as damping increases as compared to low damping ratio values.
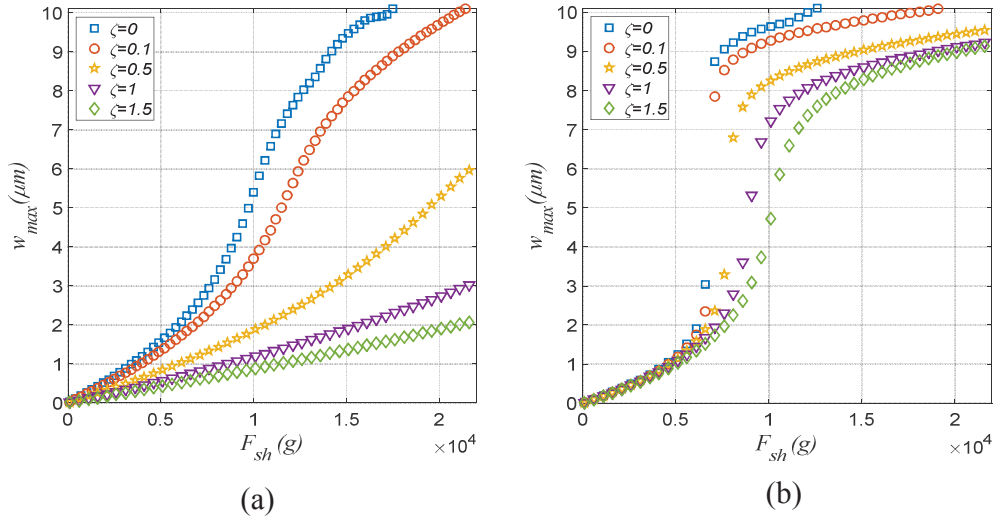
Figure 4.3: Maximum deflection versus shock amplitude for different damping ratio for shock duration of (a) 0.4 T_n (b) 4 T_n.

4.1.1.3 Effect of Initial Rise on Shock Spectrum

Now, inspecting the influence of shock duration on the maximum response of the microbeam is also considered. Figure 4.4 shows shock spectrum of the considered microbeam for low to high range of shock duration for shock amplitudes of 6,500g and 16,500g. It's clear that as shock period gets near or equal to structural natural frequency the response is getting amplified compared to higher ranges of shock, which correspond to dynamic and quasi-static respectively. Moreover, in Figure 4.4-(a) we can clearly see that at initial rise $d_0 = 4$ μm the response is lower than the other rise values. This is caused by the low shock amplitude as discussed in Figure 4.2. On the other hand, Figure 4.4-(b) shows pull-in behavior for initial rise of $d_0 = 4$ μm for shock period from 0.57 T_n to 3.1 T_n . But for higher shock values the system is critical stable. Thus, using lower shallowed arched beam rise will be efficient in case of high shock loads. And in case of low response application increasing the initial rise will cause lower response for low shock amplitudes.
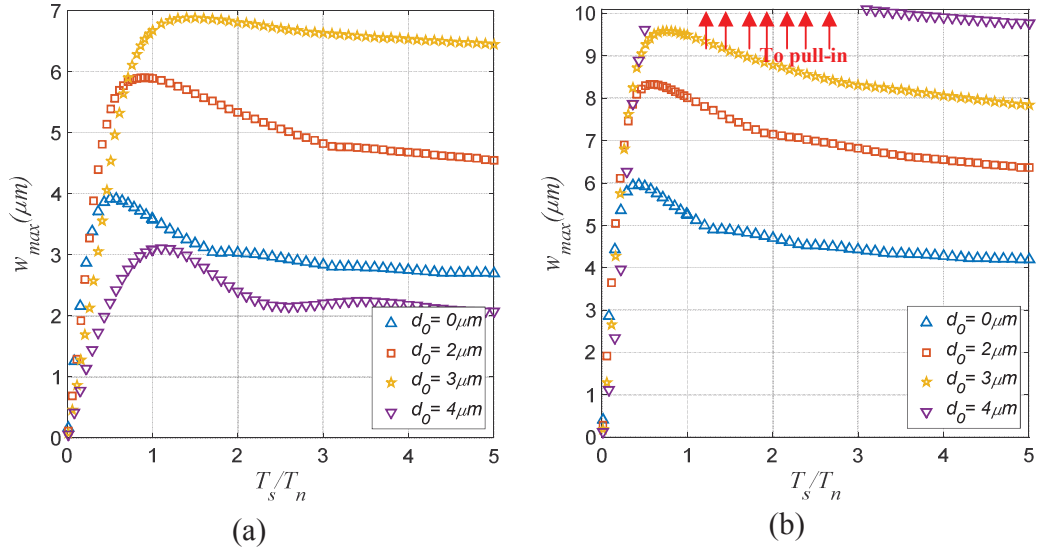
Figure 4.4: Shock spectrum for variety of inital rise values and V_{DC}=0 *Volt* (a) 6,500*g* (b) 16,500*g*.

4.2 Response Under Electrostatic DC Loads Only

DC voltages is one of the main causes of motion in MEMS devices. Thus, study their effects will be beneficial in increasing the efficiency and reliability of the devices. Figure 4.5 shows the steady state response under several V_{DC} load. Clearly, increasing the electrostatic load lead to higher steady state value.
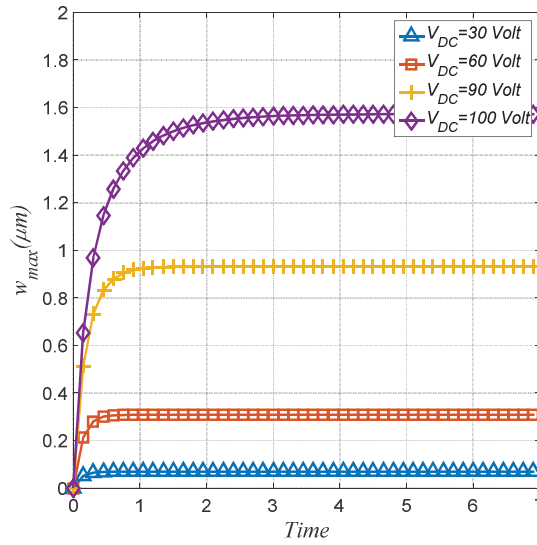
Figure 4.5: Clamped-clamped microbeam stady state response under different V_{DC} loads.

In Figure 4.6, we propose to investigate the effect of the initial rise of the shallow arch of Table 3.5 on its maximum steady state static deflection under DC load only. It is well know that the electrostatic actuation technique is one of the best method to trigger the motion in numerous MEMS devices. Thus, studying its effect would be advantageous in increasing the efficiency and reliability of such devices. We can see from the figure that increasing the shallow arch initial rise is promoting a delay in the initiation of the bi-stability regime, i.e the snap-through instability (characterized as the first slope going to infinity in Figure 4.6) and at the same time it rushes an earlier occurrence of the pull-in instability (described as the second slope going to infinity in the same figure). This actually demonstrates that the stiffness of the initially curved beam rises before the snap-through instability and then decreases in the post-snapped position with the increase of the beam initial rise value. This consequence would be very essential in the upcoming sections when investigating the influence of the beam initial rise on its structural response under the combined effect of the DC load and mechanical shaking waves.
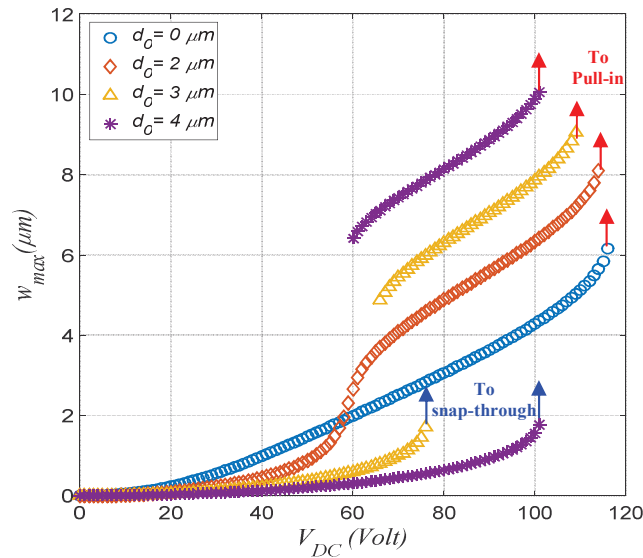
Figure 4.6: Variation of the shallow arch maximum static deflection with the DC voltagres and for different beam initial rise.

Chapter 5 : MEMS ARCH RESPONSE UNDER COMBINED EFFECTS OF MECHANICAL SHOCK WAVE AND ELECTROSTATIC LOAD

In this chapter, the effects of changing the initial rise of shallow arched microbeams on the behavior of the structure under combined of mechanical sock and electrostatic loads will be investigated. First, we will observe the of response of microbeams under constant half sine shock force at two shock durations for range of V_{DC} loads at varying initial rise. Second, the microbeam behavior under constant electrostatic loads with range of half sine shock force with two shock durations will be studied. Shock durations will be representing dynamic and quasi-statics reigns. Next, some plots representing shock spectrum under different electrostatic load and variety of initial rise values will be established. Finally, stability plots will be generated to show the maximum allowable combination of shock and electrostatic loads before the system fails due to stiction or short circuit and snap-though appearing points.

5.1 Analysis of Initial Rise Value with Combined Load

In this section, we investigate in-depth the dynamic response of the shallow arch when subjected simultaneously to a DC load and a mechanical shock wave as it is the case in numerous operating MEMS devices under a sudden drop. The motivation behind this is that it represents a good numerical tool for the improvement and optimization of MEMS arches to be used as bi-stable shock sensors or even to make them more and more reliable to shaking environments. Figures 5.1-5.4 is displaying the shallow arch maximum mid-point dynamic deflection for various initial rise values, respectively. All the figures are assuming a combined

effect of an actuating DC load along with a shock wave of various amplitude and considering two shock pulse durations of $0.4T_n$ and $4T_n$. Figure 5.1-(a) and (b) show the case of a straight microbeam. Clearly from the figure shows that the straight microbeam deflection shows only one stable state and it changes nonlinearly with the shock amplitude for both assumed cases of shock durations. Also, we can say that operating the straight microbeam at low DC voltages promotes larger beam deflection without any possibility of pull-in instability, except at higher DC load voltage, example the 90 *Volt*, the beam experiences a dynamic pull-in instability under the effect of both DC voltage and shock loads. This instability is happening earlier and for low values of shock loads for the case of shock duration near the natural period of the micro-structure (case of $T_s = 0.4T_n$). This is mostly due to the fact that the mechanical shock load with lower duration has shorter-time effect on the system mostly owning high stiffness, i.e. low natural period, and then intense vibration would be more prominent.

On the other hand, when assuming an initial curvature, the combined effect of both excitations is showing more exciting structural behaviors, Figures 5.2 and 5.4. For example, when observing carefully these figures which are all assuming non-zero initial rise values, one can conclude that increasing the DC electrostatic force further while assuming low shock amplitudes can lead to an earlier dynamic snap-through sudden instability. From the same figures, we can realize that the arch beam undergoes a sudden snapping instability for the case of $T_s = 4T_n$, Figures 5.2-(b), 5.3-(b) and 5.4-(b), and in contrary, when assuming $T_s = 0.4T_n$, the shallow arch experience a continuous snap-through instability with the increase of the shock load amplitude, Figures 5.2-(a), 5.3-(a) and 5.4-(a). These results indicate that initially curved structures respond to mechanical shock waves in two different manners: either quasi-statically for the case of $T_s = 4T_n$ as shown in Figures 5.2-(b), 5.3-(b) and 5.4-(b), making them more

prominent to be used as bi-stable g-sensors, or dynamically for the case of $T_s=0.4T_n$ as shown in Figures 5.2-(a), 5.3-(a) and 5.4-(a), endorsing them to more suitable in certain applications requiring large stroke for high g-sensing purposes.
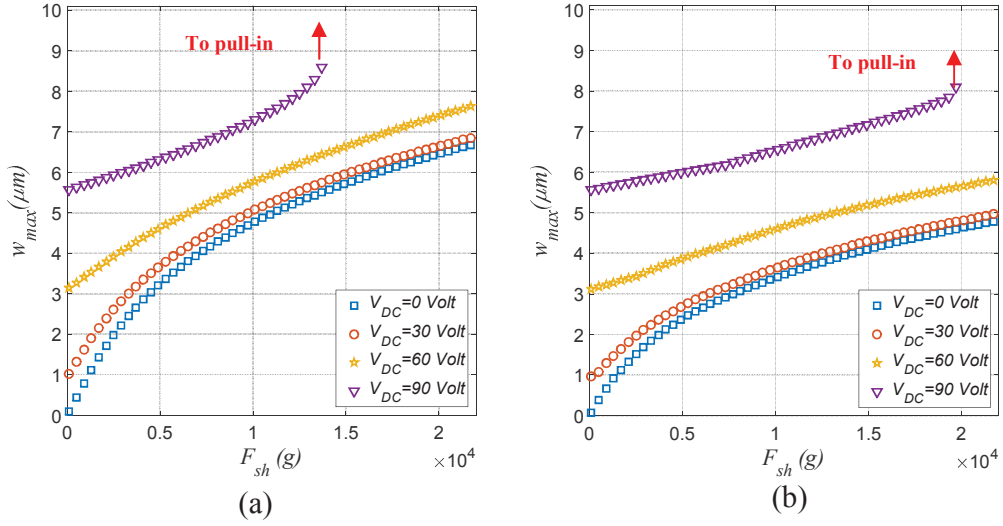
Figure 5.1: Static deflection versus shock amplitude for different electrostatic loads at $d_0= 0$ μm for shock duration of (a) 0.4 T_n (b) 4 T_n.
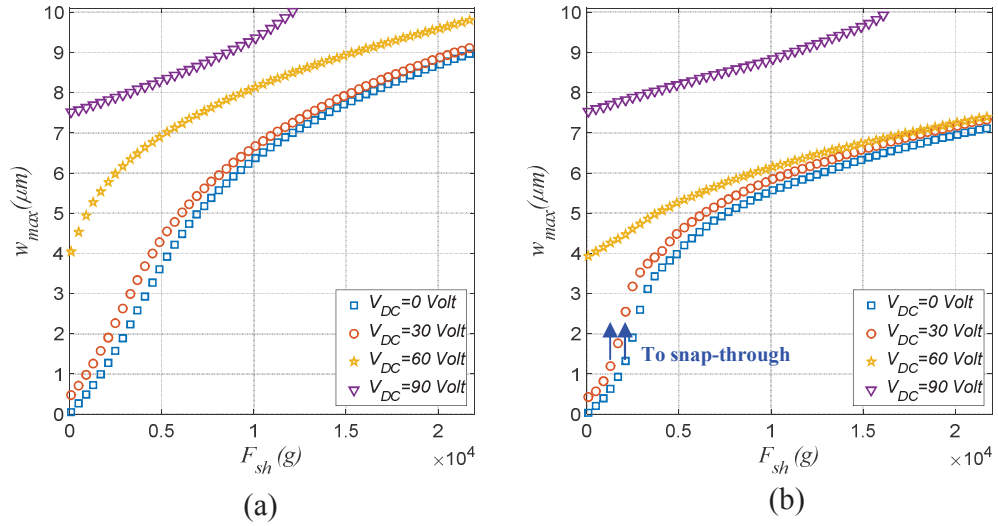
Figure 5.2: Static deflection versus shock amplitude for different electrostatic loads at $d_0= 2$ μm for shock duration of (a) 0.4 T_n (b) 4 T_n.

58
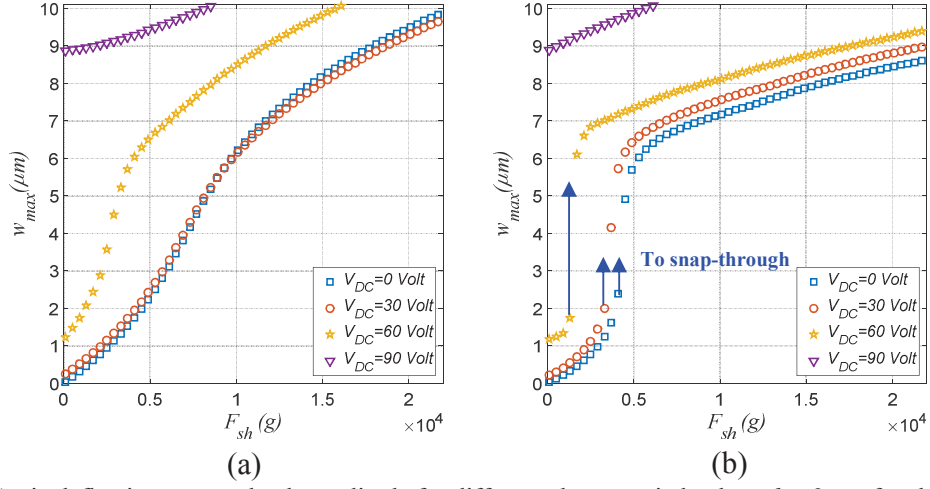
Figure 5.3: Static deflection versus shock amplitude for different electrostatic loads at $d_0 = 3$ μm for shock duration of (a) 0.4 T_n (b) 4 T_n.
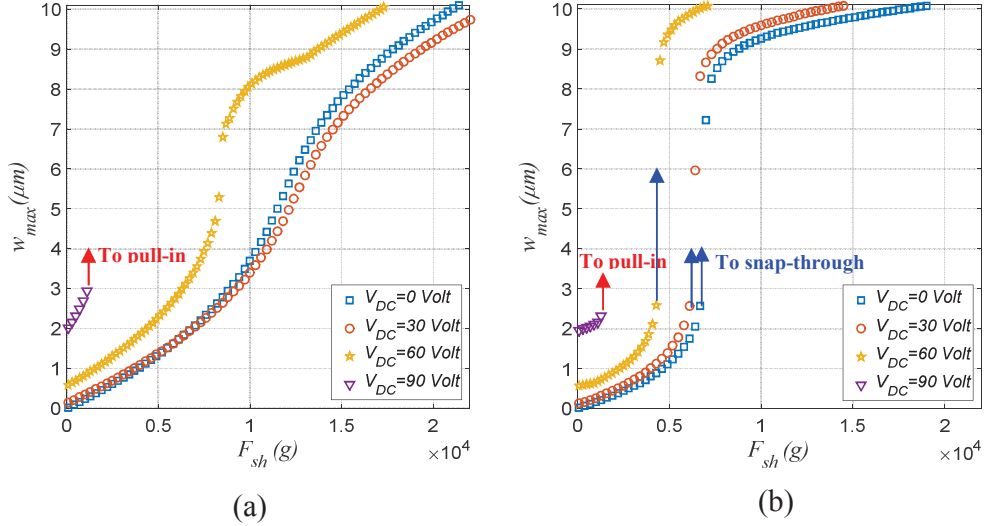
Figure 5.4: Static deflection versus shock amplitude for different electrostatic loads at $d_0 = 4$ μm for shock duration of (a) 0.4 T_n (b) 4 T_n.

In addition, Figures 5.2-5.4 shows that increasing the shock wave amplitude assuming high DC voltages can cause a sudden collapse of the system in the dynamic case, where on the other hand the system operates steadily in the quasi-static case for high DC and shock wave amplitudes. Commonly in MEMS devices, it was previously demonstrated that adding electrostatic force to a shock wave lead systematically to the initiation of an earlier pull-in instability in both dynamic and quasi-static regimes. Furthermore, Figures 5.2-5.4 are showing that increasing both DC and shock amplitudes, for both cases of shock durations, the shallow

59

arch is experiencing the dynamic snap-through instability more earlier when decreasing its initial rise.

5.1.1.1 Effect of Initial Rise on Force Response

Now we propose to investigate the same combined behavior of the previous plots but while comparing the effect of initial rise values and assuming a constant DC load in each case. Accordingly, Figures 5.5-5.7 is displaying the variation of the shallow arch beam maximum dynamic deflection with the shock wave amplitude, for various initial rises and considering three different DC voltages of 30, 60 and 90 *Volt*, respectively, and two shock wave durations of $0.4T_n$, and $4T_n$. We can evidently see from Figures 5.5-(a) and (b) that increasing the rise value for small shock load amplitude and DC voltage cause a lower deflection of the shallow arch. That's is mainly attributed to the fact that more rise would result into more stiffness and hence more robustness against external excitations mostly before undergoing the snap-through behavior. In the other hand, the system is showing a different behavior when assuming higher shock loads where a micro-arch with bigger initial rise is experiencing more deflection for higher exciting loads. The reason for this is that once the arch experiences the snap-through motion, the softening effects of both beam curvature and the electrostatic forces are dictating the structural behavior of the shallow arch and hence a bi-stable system with extra initial curvature would be more closer to the lower actuating electrode and hence more prominent for higher deflection and consequently would experience first the dynamic pull-in instability. Moreover, when assuming a 60 *Volt* DC load, Figures 5.6-(a) and (b) show a clear correlation among the shallow arch initial rise value and the initiation of the snap-through instability. Both plots show that increasing the beam initial rise, the arch behavior is changing from experiencing a continuous snap-through process to a sudden snap-through occurrence. Increasing the DC load further to 90 *Volt*, Figures

60

5.7-(a) and (b), the results are indicating that increasing both arch initial rise value and DC load can cause the system to systematically undertake a pull-in stiction instability without even any possibility of a bi-stable behavior. Same figure show also that the pull-in collapse instability is arising for lower values of shock amplitudes in the dynamic case, Figure 5.7-(a) as compared to quasi-static case, Figure 5.7-(b). In conclusion, the preceding results are demonstrating that increasing both the shallow arch initial rise can cause lower maximum deflection for low shock amplitudes and could result to an earlier system snap-through and pull-in collapse instabilities. Moreover, the initially curved system is showing two fancy bi-stable behavior: a continuous and a sudden snap-through, which were shown all to be function of the DC load, the shock amplitude and duration, and essentially the beam effective stiffness i.e. its initial shape.
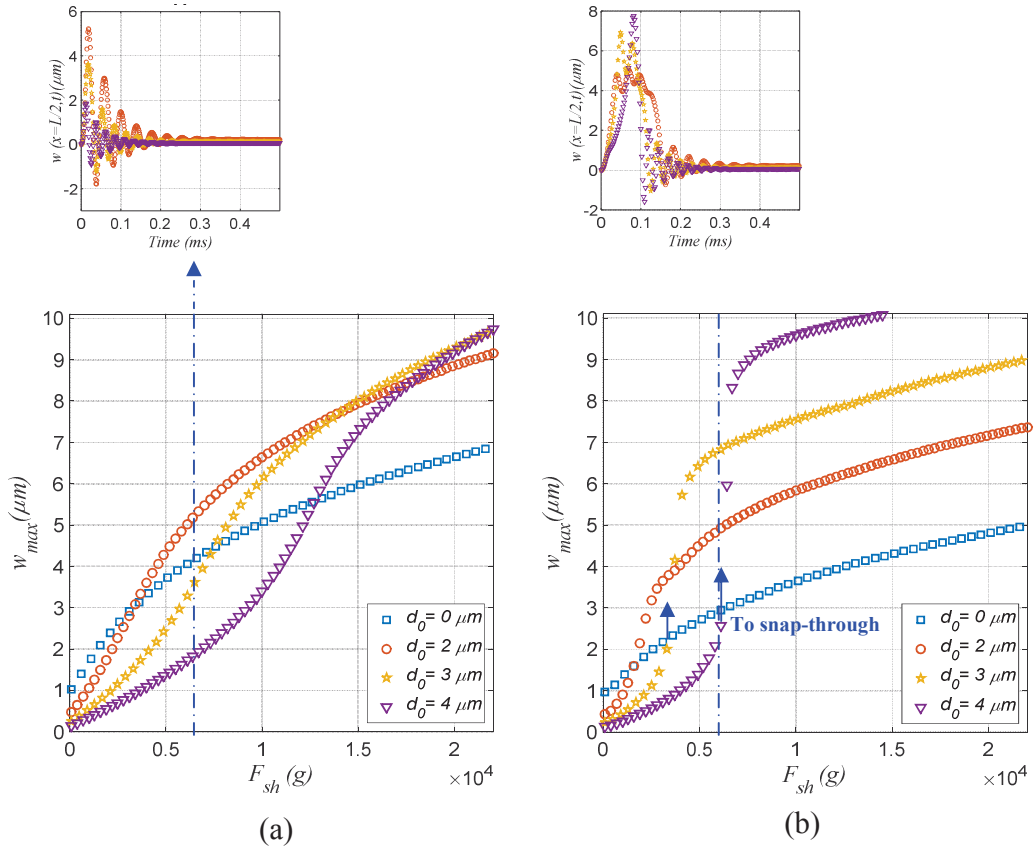
Figure 5.5: Static deflection versus shock amplitude and $V_{DC} = 30$ *Volt* for different beam initial rise for shock duration of (a) 0.4 T_n (b) 4 T_n.
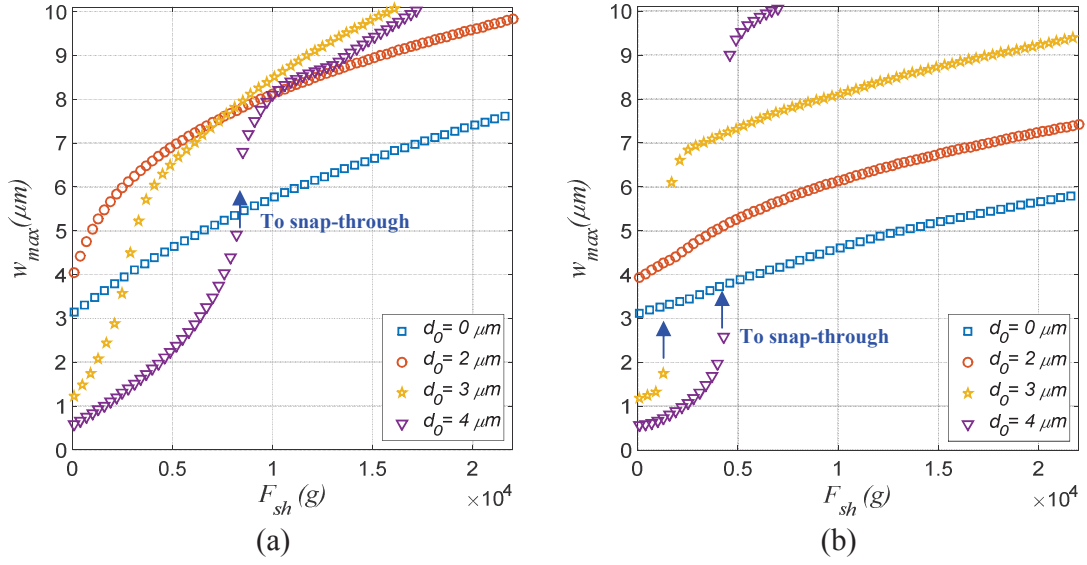
Figure 5.6: Static deflection versus shock amplitude and $V_{DC} = 60$ *Volt* for different beam initial rise for shock duration of (a) 0.4 T_n (b) 4 T_n.
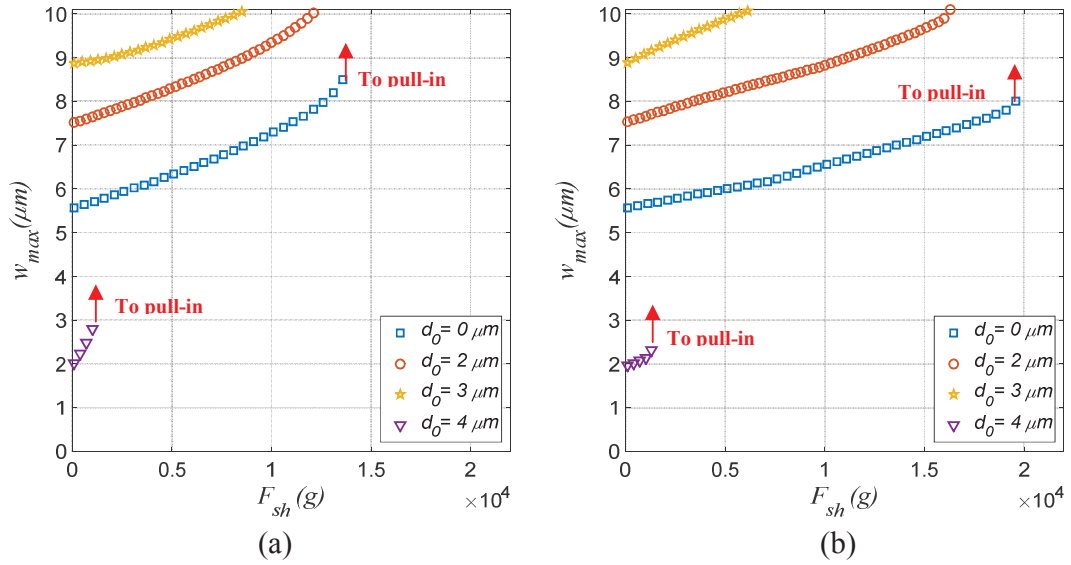
Figure 5.7: Static deflection versus shock amplitude and $V_{DC} = 90$ *Volt* for different beam initial rise for shock duration of (a) 0.4 T_n (b) 4 T_n.

5.2 Analysis of Initial Rise Value on Shock Spectrum Response

In this section we propose to analyze the effect of the shallow arch initial rise on its shock spectrum response (SSR). The SSR is a famous diagram demonstrating the variation of a system's peak dynamic response to shock load as a function of the ratio between the shock wave duration T_s to the system first natural period T_n [75]. The diagram is acquired by solving for the

maximum transient response of the investigated system while varying either the shock wave duration while keeping the system natural period constant or vice versa.

In our case, we will consider four different arch initial rise values, thus four different natural periods which are all summarized in Table 4.1. Then we vary the shock pulse duration to generate the SSR of the shallow arch of Table 3.5 assuming two different values of the shock amplitudes (F_{sh} =6,500g and F_{sh} =16,500g respectively) in each case, Figures 5.8-5.11. Starting with the straight beam case, Figures 5.8-(a) and (b), when the microbeam is subjected to a shock amplitude of 6,500g and for various DC loads, we can note from the figure that, as we raise the electrostatic voltage, the dynamic deflection of the structure considerably increases and its respective SSR peak shifts to the left. This comportment demonstrates that the mid-plane geometric stretching of the straight beam as triggered by the DC load acts here as a hardener to the microstructure. Furthermore, we can discern from Figure 5.8-(b) when we amplified the shock pulse amplitude to 16,500g, and for high DC load of 90 *Volt*, the microbeam experiences a dynamic pull-in for certain range of shock durations. This can be depicted as a dynamic pull-in zone or a failure zone. This comportment demonstrates that the actuating electrostatic load acts here as a softener to the microstructure.

Next we examine the effect of increasing the micro-arch initial rise from 0 *μm*, to 2 *μm* and 3 *μm* in Figures 5.9-5.10, respectively. We observe here a dissimilar behavior as for the straight beam case regarding the influence of the DC load in the lower range of shock durations. In fact, in these non-zero initial rise cases, as we increase the DC voltage, the dynamic deflection of the shallow arch considerably increases and its respective SSR peak shifts to the right. This performance demonstrates that the initial shape geometric nonlinearity acts here as a softener to the microstructure whose fundamental frequency is decreasing accordingly. In addition, the bi-

stable structural behavior of the shallow arch is showing to be supporting more the symmetric shape state, except for very small values of shock durations, and thus depicting a band of snap-through motion as shown by the blue arrows in Figures 5.9 and 5.10. Furthermore, as both the DC load and initial rise are increased further, the micro-arch is undergoing the pull-in instability even faster and for higher range of shock pulse durations, as exposed by the red arrows in Figures 5.9 and 5.10.

Finally, increasing further the shallow arch initial rise to 4 *μm*, as portrayed in Figure 5.11, what is interesting to realize is that for the case of high initial rise and with limited gap size, the arch would not have enough room to move from one state to the other and the arch response under high shock load is showing almost inevitable pull-in band all the way and for almost all shock durations values, Figure 5.11-(b). Whereas, for lower shock wave amplitude, Figure 5.11-(a), the arch SSR is showing three different scenarios: for zero DC load that would not initiate any static snap-through motion, the SSR is only displaying a mono-stable response of the arch for all values of shock durations. For higher DC load of 30 *Volt*, the arch SSR is showing a two snap-through responses for lower and then higher shock durations. Increasing the DC load further to 60 *Volt*, a single snap-through motion is depicted for all consider shock wave durations. Finally, for a DC value close to the pull-in instability and with the shock load amplitude, the arch doesn't have enough room to vibrate and therefore it dynamically pulls-in even for tiny shock durations, as exhibited in Figure 5.11-(a). In fact and it this regime of high initial rise, the system's response was shown to be highly sensitive to any load amplitude (shock or DC voltage), or even any variations of the shock durations.

Figure 5.8: Shock spectrum for different values of V_{DC} with $d_0 = 0$ µm and shock amplitude (a) 6,500g (b) 16,500g.
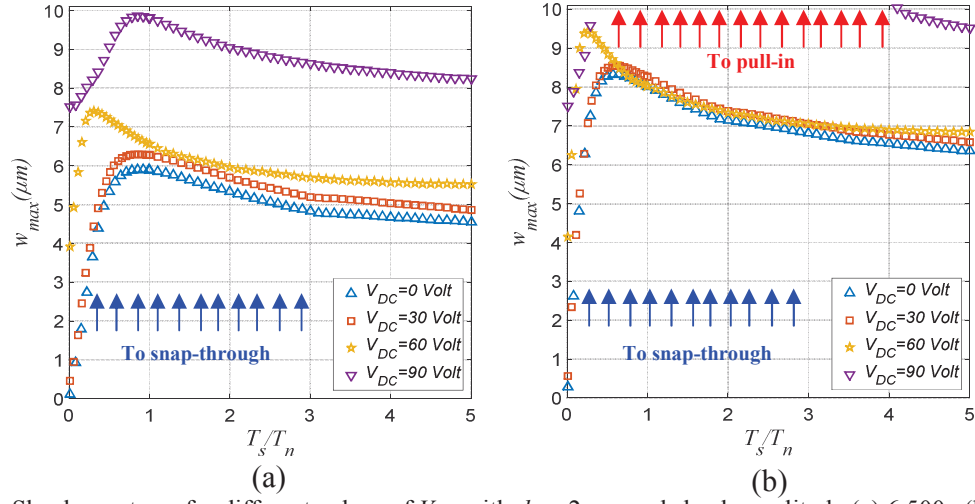
Figure 5.9: Shock spectrum for different values of V_{DC} with $d_0 = 2$ µm and shock amplitude (a) 6,500g (b) 16,500g.
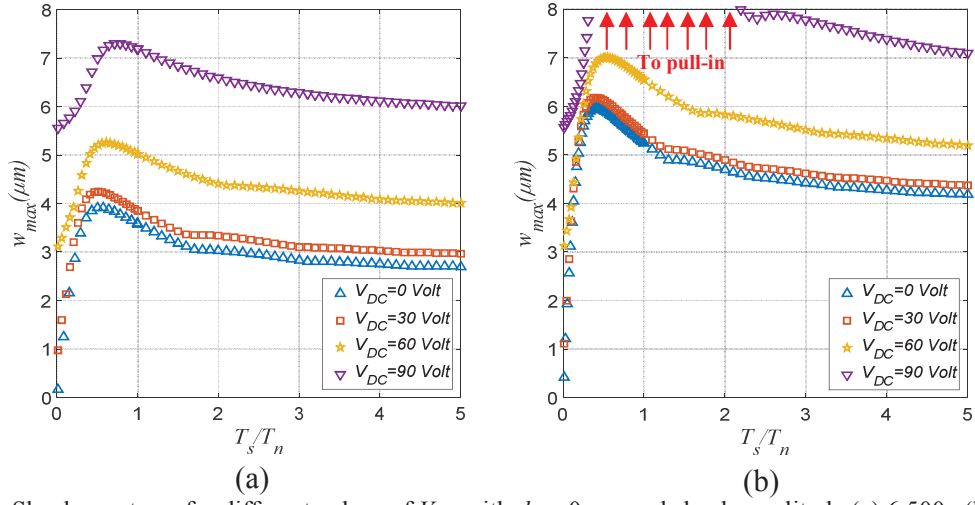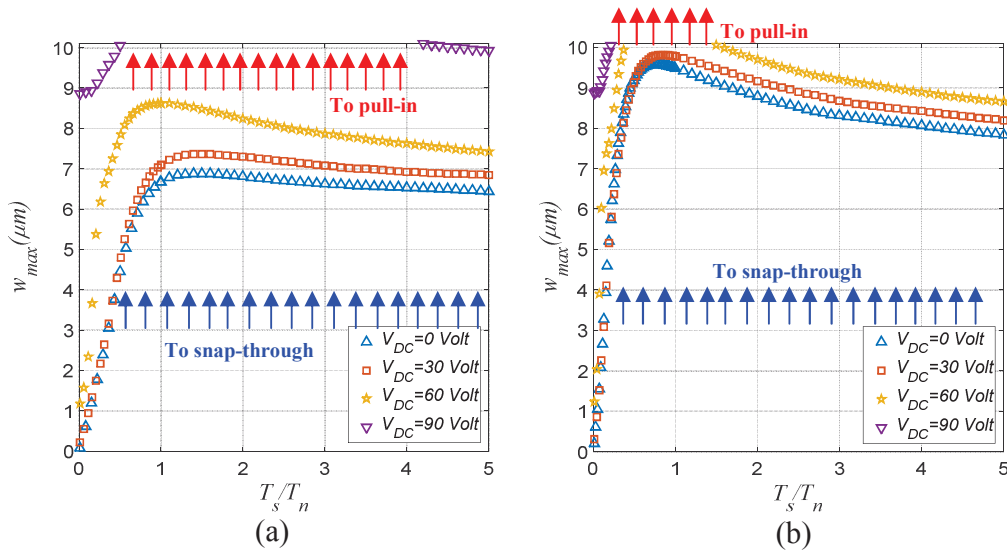

Figure 5.10: Shock spectrum for different values of V_{DC} with $d_0 = 3$ µm and shock amplitude (a) 6,500g (b) 16,500g.

65
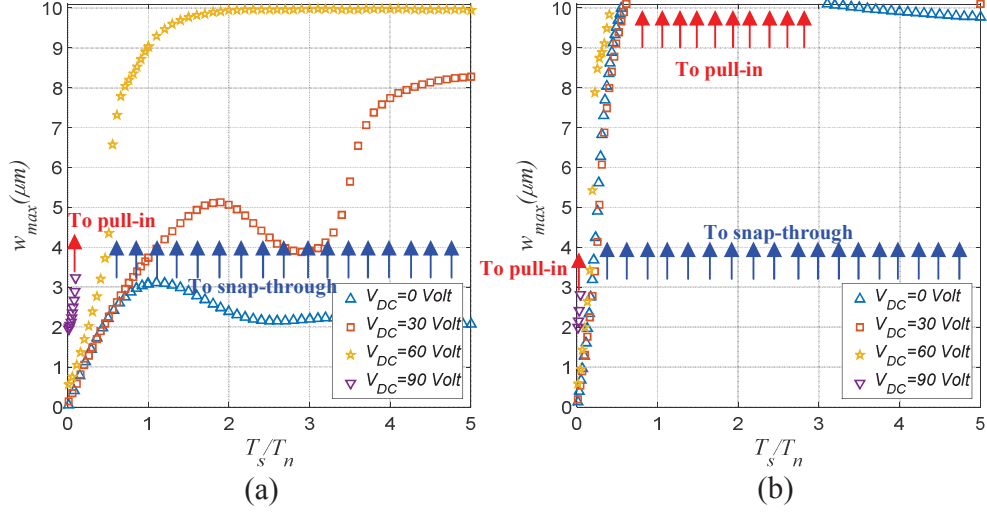
Figure 5.11: Shock spectrum for different values of V_{DC} with $d_0 = 4$ µm and shock amplitude (a) 6,500g (b) 16,500g.

5.2.1.1 Effect of Initial Rise on Shock Spectrum

Afterward, we propose to analyze the effect of changing the shallow arch initial rise on its SSR, Figures 5.12-5.14. In each diagram we assume a constant DC voltage and two distinct shock amplitudes of 6,500g and 16,500g respectively. Figures 5.12, 5.13 and 5.14 show the SSR curves for a DC load of 30 *Volt*, 60 *Volt*, and 90 *Volt*, respectively, and with various arch initial rise values. Observing from all figures that increasing the initial rise at high shock amplitude would increase the probability of observing a dynamic snap-through instability for any value of the wave durations. Although, for a higher values of the rise, for example for the initial rise of 4 *µm*, the arch tend to have lower dynamic deflections for low shock pulse durations and higher deflections for higher values of shock durations, as compared to the other initial rise values. This mainly attributed to the fact that arch possessing higher curvature would have enough band of jump between the first natural shape and its second symmetric shape as discussed previously in the static analysis. In the other hand and for high shock load, the arch would not have enough

66

range of travel for deflection, and therefore it would snap for low values of initial rises of pull-in for an additional shock load amplitude values.
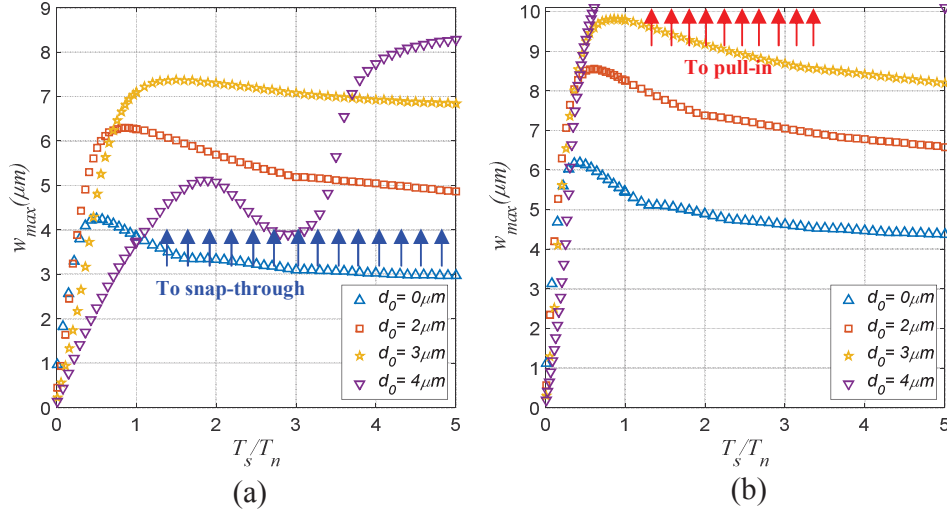
Figure 5.12: Shock spectrum for different values of beam rise under combined load of V_{DC} = 30 *Volt* and shock amplitude (a) 6,500g (b) 16,500g.

It can also be concluded that assuming an extra DC load of 60 *Volt* and 90 *Volt*, as illustrated in Figures 5.13-5.14 respectively, assuming high shock amplitudes would upsurge the system instability by causing it to either snap-through for almost all values of assumed shock durations. Nevertheless, as the ratio of T_s/T_n is converging toward the quasi-static regime, any lower initial rise values tend to show a dynamically stable state. Consequently, increasing the initial curvature of the shallow arch can cause the system to behave in a bi-stable manner (vibrating in between its two symmetric stable states), mono-stable mode (vibrating in either stable positions) or could collapse through a pull-in instability under the combined effect of shock wave duration and amplitude and the DC voltage.
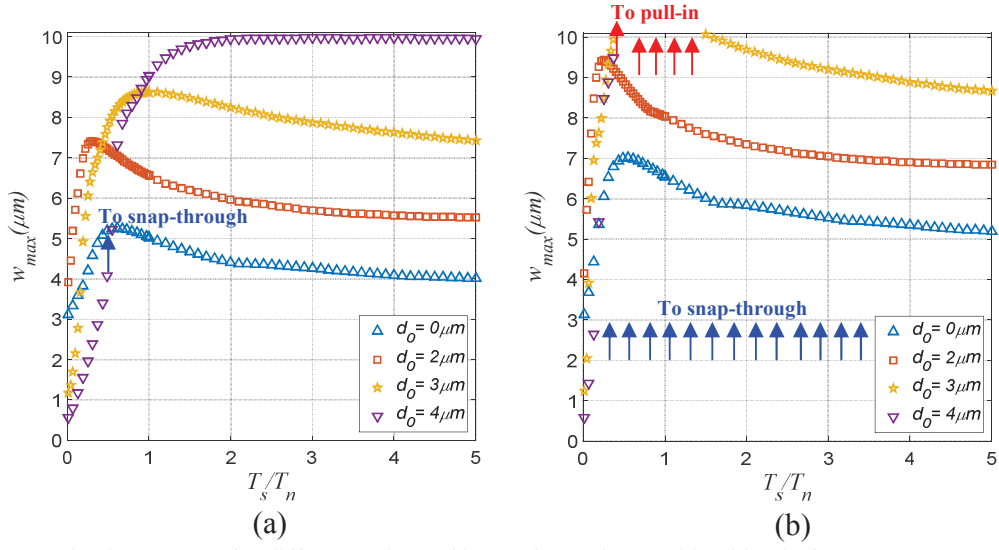
Figure 5.13: Shock spectrum for different values of beam rise under combined load of $V_{DC} = 60$ *Volt* and shock amplitude (a) 6,500g (b) 16,500g.
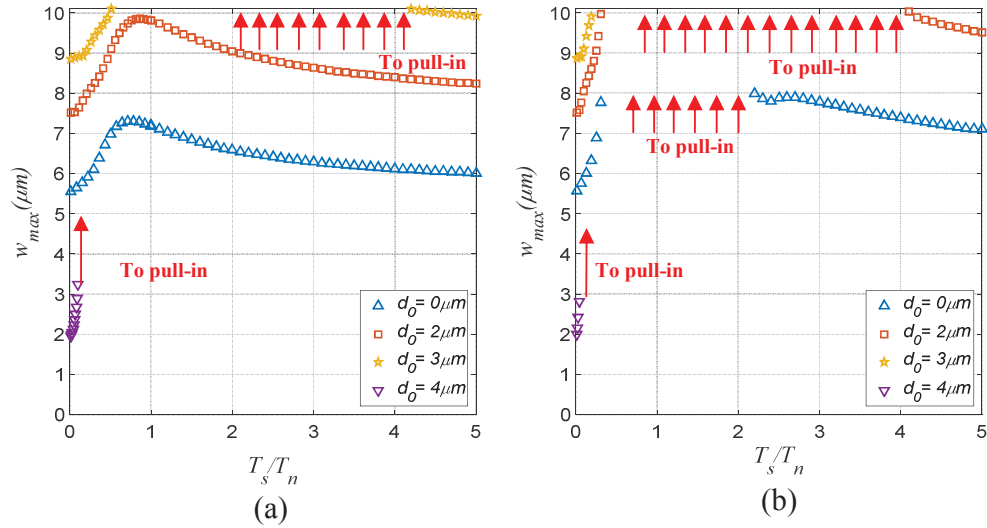
Figure 5.14: Shock spectrum for different values of beam rise under combined load of $V_{DC} = 90$ *Volt* and shock amplitude (a) 6,500g (b) 16,500g.

5.3 Limitation Analysis of Microbeam Under Combined Load

In this section, we propose to study the structural instability limitation curves of the shallow arch microbeam by investigating its maximum electrostatic/shock amplitudes that the bi-stable structure can withstand before collapsing. It is worth mentioning that the shallow arch can

either undergo a dynamic snap-through motion which represents the bi-stability or it can touch dynamically the lower electrode which characterizes the structural stiction instability. In this regards, three different values of initial rises were taken into consideration to establish the limitation curves, d_0= 2, 3 and 4μm. Figure 5.15 shows the limitation curves assuming two shock durations representing the dynamic and quasi-static regions, respectively. We can clearly comprehend from the figure the effect of increasing the initial rise which is causing the system to stick to its lower electrode (pulls-in) for low values of shock/DC amplitudes.

Furthermore, we can understand from the limitation curves for cases of d_0= 2 and 3 μm, that both cases are showing higher range of instability in the quasi-static regime, Figure 5.15-(b), as compared to their dynamic regime, Figure 5.15-(a). In contrary, the case of d_0= 4 μm is showing a differing behavior. This is mainly attributed to the assumed shock durations that depend on the natural period of the shallow arches which also vary with the beam initial rise. The more the beam initial rise increases, the more the arch will have higher frequency, and therefore the structure would feel both assumed shock durations in the dynamic regime. The same figure shows also that increasing the shallow arch initial rise can cause an early occurrence of a dynamic pull-in instability.
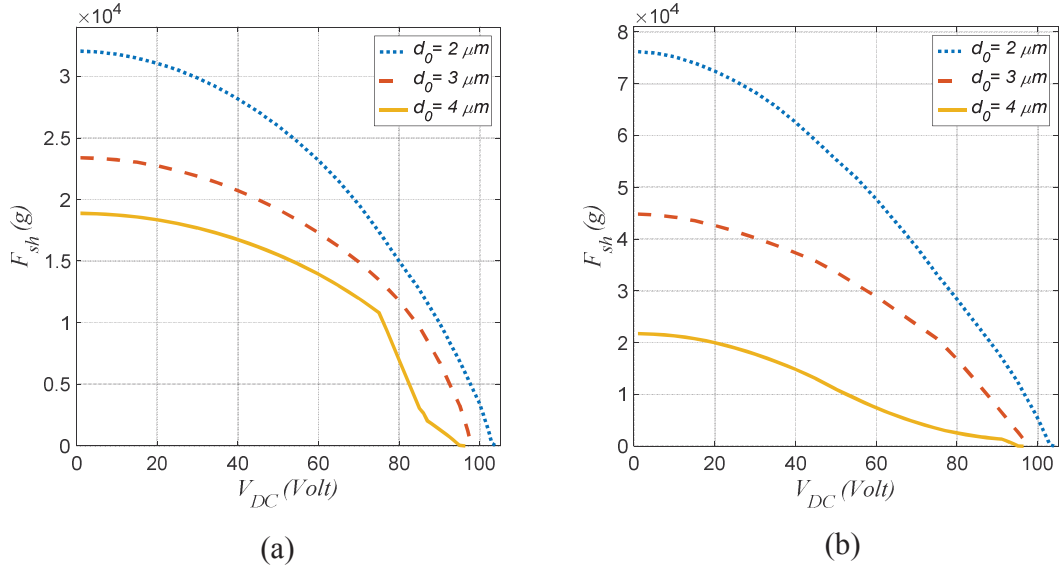
Figure 5.15: Electrostatic force versus shock amplitude depicting the dynamic pull-in instability for the MEMS arch with several initial rise and for two different shock durations of (a) T_s=0.01347 ms and (b) T_s=0.1347 ms.

5.3.1.1 Snap-through Instability Limits

Finally, we investigate the dynamic snap-through instability occurrence with the combined effect of the DC and the mechanical shock loads and compare it with the previously reported dynamic pull-in limitation curves in order to understand the dynamic bi-stability behavior of the shallow MEMS arches. Figures 5.16-(a) and (b) display the MEMS arch limitation curves depicting both the snap-through and pull-in instability occurrence for two different initial rises of d_0= 3 and 4 μm, respectively. It is clear from both graphs that increasing the amplitude of one of both combined loads, i.e, the DC or shock loads, will result in an early dynamic snap-through instability. Furthermore, operating the system at high DC load can cause instantaneous snap-through of the system even with very small shock load. In addition, it is observed that there is small range of values that will keep the system stable after the snap-through instability. This is essentially due to the fact that the dynamic snap-through voltage for a

MEMS shallow arch is always lower than or equal to the dynamic pull-in voltage as it was previously reported in [41, 44].
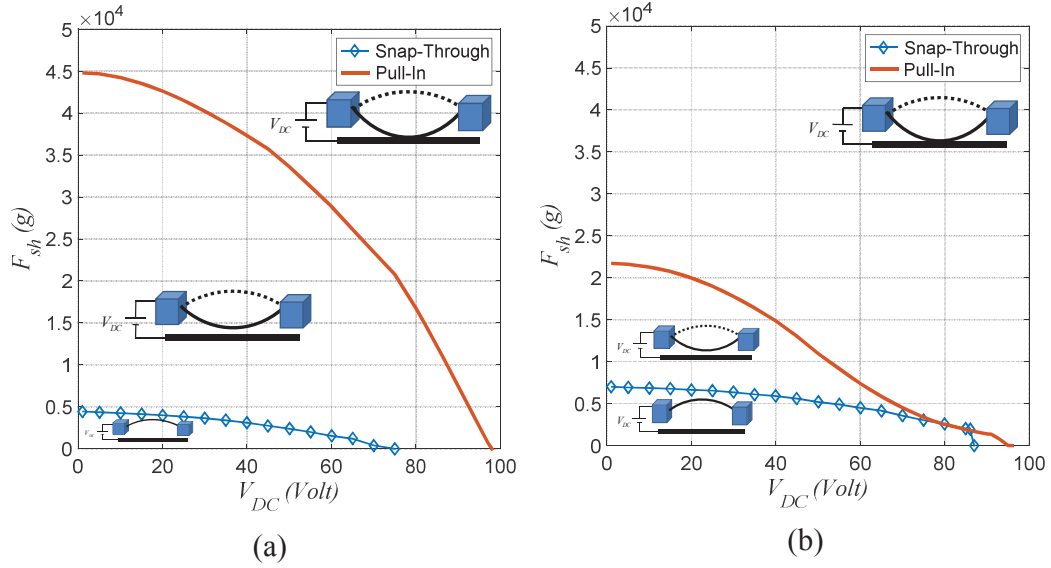
Figure 5.16: Electrostatic force versus shock amplitude depicting both dynamic snap-through and pull-in instabilities for the MEMS arch for a shock duration T_s=0.1347 *ms*, and for two initial rises: (a) d_0= 3 *μm* and (b) d_0= 4 *μm*.

Chapter 6 : SUMMARY, CONCLUSIONS AND FUTURE RESEARCH

6.1 Summary and Conclusions

To summarize the current thesis work, we first highlighted the importance of studying the reliability of MEMS based devices. Results of other researchers on the reliability of MEMS under humid condition, temperature and pressure difference were discussed. Moreover, it was found that the reliability of MEMS devices can be affected by uncontrollable factors such as the manufacturing imperfections in the micro scale which can lead to shallow arched microbeam structures.

Therefore, in this thesis, we proposed an efficient computational study/approach to simulate the vibrational response of a shallow MEMS arch under the combined effect of DC actuating load and mechanical shock waves. The numerical method was based on a Galerkin based modal reduced-order modeling (ROM). The modeshapes of a shallow arch beam are used as basis functions in the Galerkin discretization technique. We validated the ROM approach by comparing its converged results (with enough number of modes) to an ANSYS based finite element method as well as formerly published experimental data and the approach showed an excellent agreement. Also, it was demonstrated that this ROM numerical model is capable of capturing the dynamic response of shallow micro-arched under shock wave of various amplitudes and durations, in DC actuating conditions, and can consequently capture its nonlinear bi-stable structural behavior.

Moreover, a thorough examination of the effect of the initial rise value on the structural stability of clamped-clamped shallow MEMS arches under shock waves was carried out. In addition, a comprehensive parametric study was established by varying the electrostatic force value, shock amplitude and duration as the initial beam rise changes. In fact, we provided numerical solutions for the shock wave problem of electrostatically actuated shallow arches for the cases of small and large DC and shock amplitudes and assuming the dynamic (shock duration close to the system first natural period) and quasi-static (shock duration greater than its first natural period) cases. We found that higher order modes are triggered and mainly responsible for the micro-arch large deflection and therefore bi-stability nature. Moreover, it was demonstrated that adding a DC load to a shock wave would lead to the initiation of an earlier dynamic snap-through and pull-in stiction instabilities in both the dynamic and quasi-static regimes. We also showed that increasing both DC and shock amplitudes, the shallow arch might experience the dynamic snap-through instability more earlier when decreasing its initial rise and vice versa. Afterward, we investigated the micro-arch shock spectrum response (SSR), a diagram perceived as an intuitive and essential for numerous MEMS designers. We have established that increasing the shallow arch initial curvature can cause the system to behave in a bi-stable manner (vibrating in between its two symmetric stable states), mono-stable mode (vibrating in either stable positions) or could collapse through a pull-in instability under the combined effect of shock wave duration and amplitude and the DC voltage. Finally, limitation graphs were developed to show the maximum shock amplitude can be reached without causing the system to collapse considering both scenarios of dynamic pull-in or dynamic snap-through instabilities.

6.2 Future Work

There is still plenty of exploration to be discovered regarding the reliability of MEMS bi-stable based structures. Forthcoming investigations, essentially along this road, need to be established including modeling the effects impulsive shock waves on the bi-stability behavior of electrically actuated MEMS shallow arches. Therefore, in the design of such designs, both effects have to be taken into account, even if the shallow arch experiences small deflection and operates within a small range of the electrostatic voltages, to make use of or even avoid any dynamic instabilities (such as the snap-through and the pull-in), as illustrated in Figure 6.1.
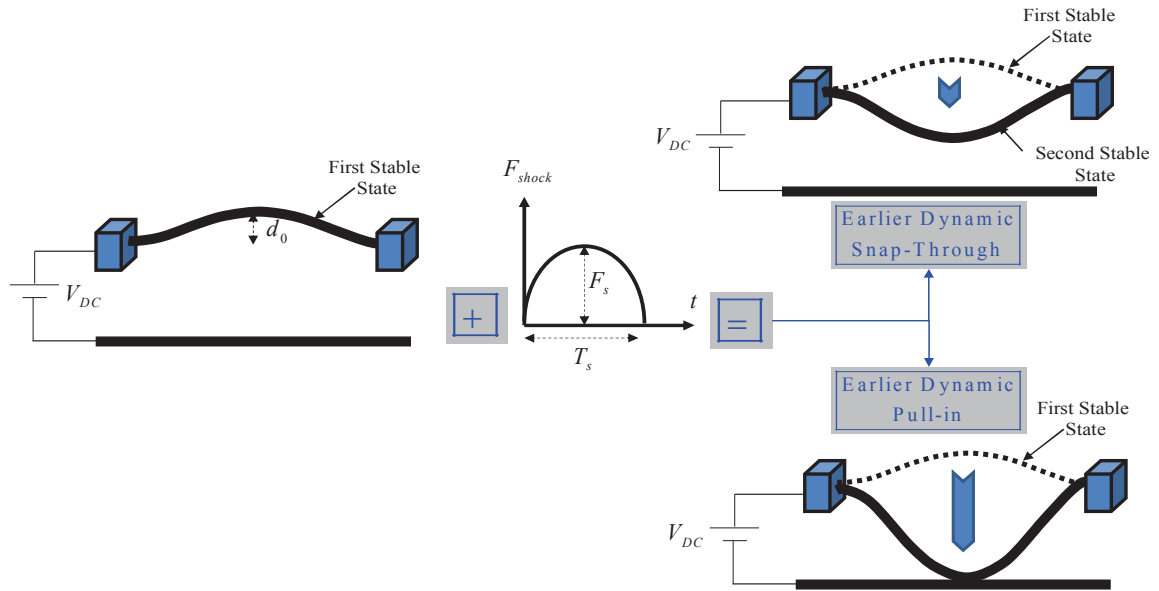
Figure 6.1: Diagram demonstrating that the association of a mechanical shock load and a nonlinear electric actuating force can be protruding some earlier structural instabilities such as snap-through and pull-in in a MEMS shallow arches.

Therefore, this work can be extended through the following proposed research ideas:

✓ Investigate more on the arched beam limitation as function of shock duration vs. electrostatic force.

✓ Study the effect of adding axial force (N) along with the arch initial curvature.

74

- ✓ Study the behavior of the limitation graphs using different shock profile such as saw tooth or step shock.

- ✓ Establish the limitation graph as function of the beam's initial rise d_0.

- ✓ Study the behavior of two arched micro beam on top of each other.

- ✓ Study the influence of arches microbeams concave downward.

REFERENCES

1.	M. I. Younis, *MEMS linear and nonlinear statics and dynamics* vol. 20: Springer Science & Business Media, 2011.
2.	U. A. Avallone, H. Baumeister Iii, and L. I. M. Sadegh, "*Standard Handbook for Mechanical Engineers*," Mechanics of Solids, vol. 3, pp. 1-2, 1987.
3.	B. Bhushan, *Introduction to tribology*: New York: John Wiley & Sons, 2002.
4.	A. S. Kurhekar, P. R. Apte, and S. P. Duttagupta, "*Design and Fabrication of Bulk Micro-machined, High Resilience, High-Q, High Tilt Angle, Low Driving Voltage, Flexure Beam Micro-mirrors on Mono-crystalline Silicon*," Silicon, vol. 8, pp. 11-24, 2016.
5.	P. F. Partnership, "*An Introduction to MEMS (Micro-Electricalmechanical Systems)*," pp. 56-59, 2002.
6.	R. Jones and M. Chapman, "*RF MEMS in mobile phones,*" RF DESIGN, vol. 28, pp. 20-24, 2005.
7.	J. Ma, "*Advanced MEMS-based technologies and displays,*" Displays, vol. 37, pp. 2-10, 2015.
8.	A. M. Boronakhin, L. N. Podgornaya, E. D. Bokhman, N. S. Filipenya, Y. V. Filatov, R. B. Shalymov, et al., "*MEMS-based inertial system for railway track diagnostics,*" Gyroscopy and Navigation, vol. 2, pp. 261-268, 2011.
9.	X. Niu, Q. Zhang, Y. Li, Y. Cheng, and C. Shi, "*Using inertial sensors of iPhone 4 for car navigation,*" pp. 555-561, 2012.
10.	L.-S. Jang, W.-H. Kan, M.-K. Chen, and Y.-M. Chou, "*Parameter extraction from BVD electrical model of PZT actuator of micropumps using time-domain measurement technique,*" Microfluidics and nanofluidics, vol. 7, pp. 559-568, 2009.
11.	F. E. H. Tay, W. Lixin, and L. H. Lee, *Production scheduling in MEMS manufacturing*: Springer, 2006.
12.	M. T. Dugger, D. B. Asay, and S. H. Kim, "MEMS Lubrication by In-Situ Tribochemical Reactions From the Vapor Phase," *Sandia National Laboratories (SNL-NM)*, Albuquerque, NM (United States)2008.
13.	P. A. Hassanpour, E. Esmailzadeh, W. L. Cleghorn, and J. K. Mills, "*Nonlinear vibration of micromachined asymmetric resonators*," Journal of Sound and Vibration, vol. 329, pp. 2547-2564, 2010.
14.	V. K. Varadan, K. J. Vinoy, and K. A. Jose, *RF MEMS and their applications*: John Wiley & Sons, 2003.
15.	H. M. Ouakad, "*The response of a micro-electro-mechanical system (MEMS) cantilever-paddle gas sensor to mechanical shock loads*," Journal of Vibration and Control, vol. 21, pp. 2739-2754, 2015.
16.	M. Gürgöze, "*On the eigenfrequencies of a cantilever beam with attached tip mass and a spring-mass system*," Journal of Sound and Vibration, vol. 190, pp. 149-162, 1996.
17.	S. D. Senturia, *Microsystem design*: Springer Science & Business Media, 2007.
18.	H. Fujita, "*A decade of MEMS and its future*," pp. 1-7, 1997.

19. A. Gusso, "*Nonlinear damping in doubly clamped beam resonators due to the attachment loss induced by the geometric nonlinearity*," Journal of Sound and Vibration, vol. 372, pp. 255-265, 2016.

20. R. Lifshitz and M. C. Cross, "*Nonlinear dynamics of nanomechanical and micromechanical resonators,*" Review of nonlinear dynamics and complexity, vol. 1, pp. 1-52, 2008.

21. T.-R. Hsu, "*Reliability in MEMS packaging*," pp. 398-402, 2006.

22. I. Stanimirovic and Z. Stanimirovic, "*Reliability of MEMS*," Microelectronics Reliability, vol. 43, pp. 1047-1048, 2011.

23. A. Somà and G. De Pasquale, "*Reliability of MEMS: effects of different stress conditions and mechanical fatigue failure detection*," pp. 72-80, 2010.

24. H. M. Ouakad and M. I. Younis, "*Modeling and simulations of collapse instabilities of microbeams due to capillary forces*," pp. 187-195, 2008.

25. C. H. Mastrangelo and C. H. Hsu, "*Mechanical stability and adhesion of microstructures under capillary forces. I. Basic theory*," Journal of Microelectromechanical systems, vol. 2, pp. 33-43, 1993.

26. W. M. van Spengen, "*MEMS reliability from a failure mechanisms perspective,*" Microelectronics Reliability, vol. 43, pp. 1049-1060, 2003.

27. P. Lall, A. S. Abrol, L. Simpson, and J. Glover, "*Reliability of MEMS devices under multiple environments*," pp. 1313-1321, 2014.

28. Y. Huang, A. S. S. Vasan, R. Doraiswami, M. Osterman, and M. Pecht, "*MEMS reliability review*," IEEE Transactions on Device and Materials Reliability, vol. 12, pp. 482-493, 2012.

29. J. Lueke, N. A. Quddus, W. Moussa, and A. Chahal, "*A parametric study of thermal effects on the reliability of RF MEMS switches*," pp. 30-31, 2005.

30. M. Hon, F. W. DelRio, C. Carraro, and R. Maboudian, "*Effects of relative humidity and actuation voltage on MEMS reliability*," 2007, pp. 367-370.

31. V. T. Srikar and S. D. Senturia, "*The reliability of microelectromechanical systems (MEMS) in shock environments*," Journal of Microelectromechanical Systems, vol. 11, pp. 206-214, 2002.

32. H. M. Ouakad, M. I. Younis, and F. Alsaleem, "*Dynamic response of an electrostatically actuated microbeam to drop-table test*," Journal of Micromechanics and Microengineering, vol. 22, pp. 095-003, 2012.

33. P. Zhang, C. He, J. Zhang, Q. Zhao, Z. Yang, D. Zhang, et al., "*Investigation of reliability of MEMS gyroscopes under different shock conditions*," pp. 441-444, 2015.

34. D. Xuran, F. Yue, L. Wenzhong, and G. Yunlong, "*Failure of a MEMS switch after environmental test,*" pp. 417-420, 2015.

35. J. Li, M. Broas, J. Makkonen, T. T. Mattila, J. Hokka, and M. Paulasto-Kröckel, "*Shock impact reliability and failure analysis of a three-axis MEMS gyroscope*," Journal of Microelectromechanical Systems, vol. 23, pp. 347-355, 2014.

36. L. Zhang, F. Yang, R. Li, T. Guan, J. He, F. S. Fu, et al., "*A novel impact tester for in situ evaluating the shock reliability of micro-structures*," 2016, pp. 942-945.

37. K. Xu, N. Zhu, X. Zhang, W. Su, W. Zhang, and Y. Hao, "*A novel shock protection method based on MEMS compliant latching stopper*," pp. 1125-1128, 2016.

38. S. Huang, X. Li, Y. Wang, J. Jiao, X. Ge, D. Lu, et al., "*A piezoresistive accelerometer with axially stressed tiny beams for both much increased sensitivity and much broadened frequency bandwidth*," vol. 1, pp. 91-94, 2003.

39. M. Naumann, J. Mehner, D. Lin, and T. F. Miller, "*Design and application of flexible stops for MEMS devices,*" pp. 168-173, 2010.

40. F. M. Alsaleem, M. I. Younis, and M. I. Ibrahim, "*A study for the effect of the PCB motion on the dynamics of MEMS devices under mechanical shock*," Journal of Microelectromechanical Systems, vol. 18, pp. 597-609, 2009.

41. H. M. Ouakad and M. I. Younis, "*On using the dynamic snap-through motion of MEMS initially curved microbeams for filtering applications*," Journal of Sound and Vibration, vol. 333, pp. 555-568, 2014.

42. J. Qiu, J. H. Lang, and A. H. Slocum, "*A curved-beam bistable mechanism*," Journal of microelectromechanical systems, vol. 13, pp. 137-146, 2004.

43. J. S. Han, C. MÃžller, U. Wallrabe, and J. G. Korvink, "*Design, simulation, and fabrication of a quadstable monolithic mechanism with X-and Y-directional bistable curved beams*," Journal of Mechanical Design, vol. 129, pp. 1198-1203, 2007.

44. H. M. Ouakad, "*An electrostatically actuated MEMS arch band-pass filter,*" Shock and Vibration, vol. 20, pp. 809-819, 2013.

45. L. Ruzziconi, S. Lenci, and M. I. Younis, "*An imperfect microbeam under an axial load and electric excitation: nonlinear phenomena and dynamical integrity*," International Journal of Bifurcation and Chaos, vol. 23, pp. 135-026, 2013.

46. I.-H. Hwang, Y.-S. Shim, and J.-H. Lee, "*Modeling and experimental characterization of the chevron-type bi-stable microactuator*," Journal of Micromechanics and Microengineering, vol. 13, pp. 948-951, 2003.

47. L. Ruzziconi, A. M. Bataineh, M. I. Younis, W. Cui, and S. Lenci, "*Nonlinear dynamics of an electrically actuated imperfect microbeam resonator: experimental investigation and reduced-order modeling*," Journal of micromechanics and microengineering, vol. 23, pp. 012-075, 2013.

48. J. F. Rhoads, S. W. Shaw, and K. L. Turner, "*The nonlinear response of resonant microbeam systems with purely-parametric electrostatic actuation*," Journal of Micromechanics and Microengineering, vol. 16, pp. 890-892, 2006.

49. M. T. A. Saif, "*On a tunable bistable MEMS-theory and experiment*," Journal of microelectromechanical systems, vol. 9, pp. 157-170, 2000.

50. A. H. Nayfeh, *Nonlinear interactions*: Wiley, 2000.

51. A. H. Nayfeh, M. I. Younis, and E. M. Abdel-Rahman, "*Reduced-order models for MEMS applications,*" Nonlinear dynamics, vol. 41, pp. 211-236, 2005.

52. V. V. Zozulya and A. Saez, "*High-order theory for arched structures and its application for the study of the electrostatically actuated MEMS devices*," Archive of Applied Mechanics, vol. 84, pp. 1037-1055, 2014.

53. A. M. Bataineh and M. I. Younis, "*Dynamics of a clamped–clamped microbeam resonator considering fabrication imperfections,*" Microsystem Technologies, vol. 21, pp. 2425-2434, 2015.

54. H. M. Ouakad and M. I. Younis, "*The dynamic behavior of MEMS arch resonators actuated electrically*," International Journal of Non-Linear Mechanics, vol. 45, pp. 704-713, 2010.

55. A. H. Ramini, Q. M. Hennawi, and M. I. Younis, "*Theoretical and Experimental Investigation of the Nonlinear Behavior of an Electrostatically Actuated In-Plane MEMS Arch*," Journal of Microelectromechanical Systems, vol. 25, pp. 570-578, 2016.

56. H. Farokhi, M. H. Ghayesh, and S. Hussain, "*Pull-in characteristics of electrically actuated MEMS arches*," Mechanism and Machine Theory, vol. 98, pp. 133-150, 2016.

57. H. M. Ouakad, "*Electrostatic fringing-fields effects on the structural behavior of MEMS shallow arches,*" Microsystem Technologies, pp. 1-9, 2016.

58. H. M. Ouakad, H. M. Al-Qahtani, and M. A. Hawwa, "*Influence of squeeze-film damping on the dynamic behavior of a curved micro-beam*," Advances in Mechanical Engineering, vol. 8, pp. 120-134, 2016.

59. H. M. Ouakad, "*Nonlinear structural mechanics of micro and nano systems*," Ph.D Dissertation, Mechanical engineering, STATE UNIVERSITY OF NEW YORK AT BINGHAMTON, 2010.

60. S. Krylov and R. Maimon, "*Pull-in dynamics of an elastic beam actuated by distributed electrostatic force*," pp. 1779-1787, 2003.

61. F. M. Alsaleem, M. I. Younis, and H. M. Ouakad, "*On the nonlinear resonances and dynamic pull-in of electrostatically actuated resonators*," Journal of Micromechanics and Microengineering, vol. 19, pp. 013-045, 2009.

62. J. Pitarresi, B. Roggeman, S. Chaparala, and P. Geng, "*Mechanical shock testing and modeling of PC motherboards*," vol. 1, pp. 1047-1054, 2004.

63. A. H. Nayfeh and P. F. Pai, *Linear and nonlinear structural mechanics*: John Wiley & Sons, 2008.

64. W. R. Hamilton, "*On a general method in dynamics; by which the study of the motions of all free systems of attracting or repelling points is reduced to the search and differentiation of one central relation, or characteristic function*," Philosophical transactions of the Royal Society of London, vol. 124, pp. 247-308, 1834.

65. W. R. Hamilton, "*Second essay on a general method in dynamics*," Philosophical Transactions of the Royal Society of London, vol. 125, pp. 95-144, 1835.

66. M. I. Younis, E. M. Abdel-Rahman, and A. Nayfeh, "*A reduced-order model for electrically actuated microbeam-based MEMS*," Journal of Microelectromechanical systems, vol. 12, pp. 672-680, 2003.

67. A. H. Nayfeh and D. T. Mook, *Nonlinear oscillations*: John Wiley & Sons, 2008.

68. M. I. Younis, R. Miles, and D. Jordy, "*Investigation of the response of microstructures under the combined effect of mechanical shock and electrostatic forces*," Journal of Micromechanics and Microengineering, vol. 16, pp. 24-63, 2006.

69. W. Lacarbonara and G. Rega, "*Resonant non-linear normal modes. Part II: activation/orthogonality conditions for shallow structural systems*," International Journal of Non-Linear Mechanics, vol. 38, pp. 873-887, 2003.

70. P. J. P. Goncalves, M. J. Brennan, and S. J. Elliott, "*Numerical evaluation of high-order modes of vibration in uniform Euler–Bernoulli beams,*" Journal of sound and vibration, vol. 301, pp. 1035-1039, 2007.

71. *Mathematica*, "Wolfram Research, Inc.," vol. Version 10.0, ed. Champaign, Illinois: Wolfram Research, Inc., 2014.

72. M. I. Younis, F. Alsaleem, and D. Jordy, "*The response of clamped–clamped microbeams under mechanical shock*," International Journal of Non-Linear Mechanics, vol. 42, pp. 643-657, 2007.

73. S. Krylov, B. R. Ilic, D. Schreiber, S. Seretensky, and H. Craighead, "*The pull-in behavior of electrostatically actuated bistable microstructures*," Journal of Micromechanics and Microengineering, vol. 18, pp. 026-055, 2008.

74. *ANSYS*, "Mechanical APDL," vol. R 15.0, ed: www.ansys.com, 2013.

75. R. L. Wells, "*Using shock response spectra to design motion control profiles for flexible structures*," Journal of Vibration and Control, vol. 7, pp. 905-921, 2001.

VITAE

Name   : Jihad Erfan AlQasimi

Nationality   : Saudi Arabian

Email   : jeqasimi@kfupm.edu

Address   : KFUPM – Dhahran – Saudi Arabia

Academic Background   :

- M.Sc Mechanical Engineering: King Fahd University of Petroleum and Minerals

    (KFUPM), Dhahran, Saudi Arabia

    May 2017.

- B.Sc Mechanical Engineering: King Fahd University of Petroleum and Minerals

    (KFUPM), Dhahran, Saudi Arabia

    May 2015.